Catalysis Today xxx (2016) xxx–xxx

Contents lists available at ScienceDirect

Catalysis Today

journal homepage: www.elsevier.com/locate/cattod

# Recent developments in hybrid iron oxide–noble metal nanocatalysts for organic reactions

Hyunje Woo, Kang Hyun Park*

*Department of Chemistry and Chemistry Institute for Functional Materials, Pusan National University, Busan 609-735, Republic of Korea*

ARTICLE INFO

*Article history:*
Received 11 September 2015
Received in revised form
31 December 2015
Accepted 25 January 2016
Available online xxx

*Keywords:*
Hybrid
Nanoparticles
Catalyst
Iron oxide
Noble metal

ABSTRACT

A review of recent developments in the synthesis of hybrid iron oxide–noble metal nanocomposites and their application to various organic reactions is presented herein. Focus is placed on various strategies for achieving (1) Au nanoparticles (NPs) on $Fe_3O_4$@polymer catalysts, (2) optimized dispersion and stability of $Fe_3O_4$/Pd catalysts, (3) Au NPs supported on $Fe_2O_3$–graphene oxide hybrid nanosheets and (4) rose-like Pd–$Fe_3O_4$ hybrid nanocomposite-supported Au nanocatalysts. Further application of such hybrid nanocomposites as catalysts for various organic reactions is discussed in brief.



## 1. Introduction

In recent years, numerous strategies have been attempted for the design of hybrid nanostructures that combine the physical and chemical properties of each component [1–9]. Many studies have discussed the syntheses of such multicomponent nanostructures with increased functionality [10–20]. The multicomponent functions combined with the enhanced chemical and physical properties make the hybrid nanostructures suitable research targets for magnetic, plasmonic and semiconducting explorations [21–25].

The design of iron oxide nanoparticles (IONPs) has gained particular attention because of fundamental scientific interest in various cutting-edge technological applications of these species, including their use as magnetic storage media, [26] in biosensing [27] and medical applications [28,29] and as contrast agents in magnetic resonance imaging [30–33]. Thus, there has been a drive toward the synthesis of IONPs with controlled size, composition and surface properties in the subjects of extensive interdisciplinary research [34,35]. It is well known that IONPs exhibit the tendency to cluster, aggregate and lose their magnetic properties when applied in solution and in biological systems. To enhance the stability of these nanoparticles (NPs), intensive effort has been devoted to the development of hybrid nanocomposites to enable functionalization of the surfaces of IONPs and develop new design strategies for hybrid nanocomposites [36–42].

Hybrid nanocomposites are efficient catalysts for a wide range of industrially relevant organic transformations. For example, palladium and gold NPs have attracted attention as catalysts for carbon–carbon coupling reactions, reduction of 4-nitrophenol and a series of other reactions [43–53]. Magnetic NPs or nanocomposites are considered as ideal supports because they efficiently immobilize metal NPs and circumvent the complications of filtration (such as loss of catalyst, oxidation of sensitive metal complexes and usage of additional solvents for precipitation steps).

In this review, we focus on recent developments in the synthesis of hybrid iron oxide–noble metal nanocomposites and various strategies for achieving (1) Au NPs on $Fe_3O_4$@polymer catalysts, (2) optimized dispersion and stability of $Fe_3O_4$/Pd catalysts, (3) Au NPs supported on $Fe_2O_3$–graphene oxide (GO) hybrid nanosheets and (4) rose-like Pd–$Fe_3O_4$ hybrid nanocomposite-supported Au nanocatalysts (Scheme 1). Further application of such hybrid nanocomposites as catalysts to various organic reactions is also discussed in brief.

## 2. Au NPs on $Fe_3O_4$@polymer catalysts [54]

Core–shell nanocomposites have recently emerged as promising catalysts, where the shell not only protects the core from oxidation, but also facilitates surface modification and

* Corresponding author. Fax: +82 51 980 5200.
*E-mail address:* chemistry@pusan.ac.kr (K.H. Park).

http://dx.doi.org/10.1016/j.cattod.2016.01.030
0920-5861/

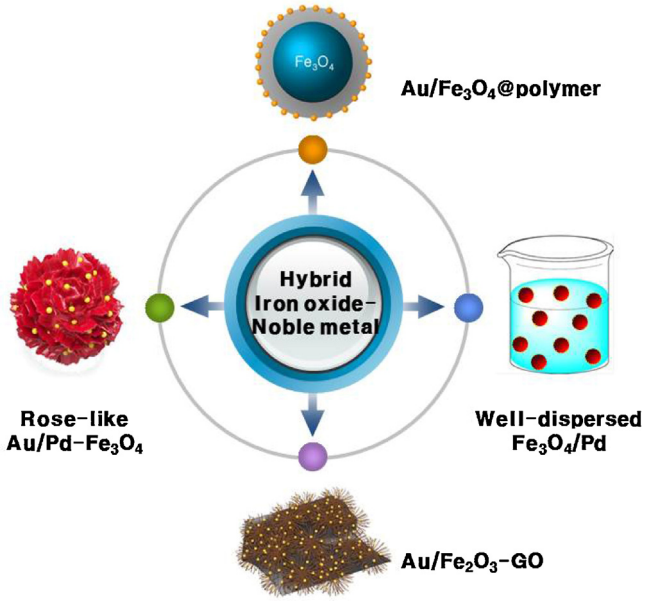


**Scheme 1.** Hybrid iron oxide–noble metal nanocomposites.

functionalization to overcome problems caused by oxidation and aggregation of IONPs. These catalysts include metal oxides such as $SiO_2$, $TiO_2$, and $Al_2O_3$, organic monolayers, and polymers [55–66]. We synthesized hybrid Au NPs on $Fe_3O_4$ microspheres, and then coated these $Fe_3O_4$ microspheres with a polymer to facilitate loading of the Au NPs and to prevent aggregation and oxidation of the $Fe_3O_4$ microspheres (Scheme 2) [54].

Scheme 2 shows the total synthesis of the $Fe_3O_4$@polymer/Au catalyst. $Fe_3O_4$ microspheres were synthesized using the solvothermal method [61,62]. This comprised the partial reduction of $FeCl_3$ with ethylene glycol as a solvent, sodium acetate as a reducing agent and trisodium citrate ($Na_3Cit$) as an electrostatic stabilizer at 200 °C. The resulting $Fe_3O_4$ microspheres are shown in Fig. 1a, demonstrating their spherical morphology with a rough surface and an average diameter of 142 nm (Fig. 2b). The $Fe_3O_4$ microspheres consisted of aggregates of small magnetite particles with a mean size of 3 nm, as observed by transmission electron microscopy (TEM) (Fig. 1b). Au NPs with a diameter of 18 nm (Fig. 2b) were immobilized on the $Fe_3O_4$@polymer microspheres through hydrogen bonding between the ester groups in the polymer and the Au precursors (Fig. 1c and d). The polymerization was carried out by using the hydrophobic monomer ethylene glycol dimethacrylate (EGDMA) as a cross-linker with the hydrophilic monomer methacrylic acid (MAA) to increase the hydrophilicity of the $Fe_3O_4$@polymer microspheres, thereby generating $Fe_3O_4$@P(EGDMA-co-MAA) core–shell microspheres. The TEM image of the $Fe_3O_4$@P(EGDMA-co-MAA) microspheres in Fig. 1b shows a well-defined core–shell structure, with a black core and a gray shell, without the appearance of any secondary polymer as shown in Fig. 1b. Because the $Fe_3O_4$ microspheres had carboxyl groups on their surfaces due to the use of $Na_3Cit$ in the magnetic synthetic system, the synergetic hydrogen bonds formed between the carboxyl groups and ester groups, as well as between the carbonyl groups and hydroxyl groups, were strong enough to synthesize P(EGDMA-co-MAA) on the magnetite surface. Thus, hydrogen bond interactions played an important role during the coating of the polymer onto the $Fe_3O_4$ microspheres [61,62]. X-ray diffraction (XRD) (Fig. 2a) was used to identify the crystal phase of the $Fe_3O_4$ spherical aggregates and $Fe_3O_4$@P(EGDMA-co-MAA)/Au. Specifically, the patterns could be assigned to the (2 2 0), (3 1 1), (4 0 0), (4 2 2), (5 1 1), (4 4 0), and (5 3 3) reflections of the cubic spinel structure of $Fe_3O_4$ (JCPDS No. 19-0629) and the (1 1 1), (2 0 0), (2 2 0), and (3 1 1) reflections of face centered cubic (fcc) Au (JCPDS No. 04-0784). The elemental compositions of the $Fe_3O_4$@P(EGDMA-co-MAA)/Au catalyst were obtained using energy-dispersive X-ray spectroscopy (EDS) (Fig. 2c). The superconducting quantum interference device (SQUID) data (Fig. 2d) shows the magnetic curves as a function of the applied field at 300 K. The saturation magnetization value of $Fe_3O_4$@P(EGDMA-co-MAA)/Au was about 45.3 emu $g^{-1}$, which was a similar to that of $Fe_3O_4$@P(EGDMA-co-MAA) at about 46.4 emu $g^{-1}$. There was no drastic decrease of the magnetization after loading of the Au NPs. Moreover, the remanence and coercivity of the $Fe_3O_4$ microspheres were both close to zero, indicating superparamagnetism.

The UV/vis absorption of the reaction mixture was monitored with time during the catalytic reduction of 4-nitrophenol (Fig. 3). Notably, the absorption of 4-nitrophenol at 400 nm decreased rapidly with a concomitant increase in the intensity of the peak at 300 nm, which is attributed to the product of the reduction, 4-aminophenol. In control experiments, only the $Fe_3O_4$@P(EGDMA-co-MAA) microspheres were used as the catalyst; no reaction was observed (entry 1, Table 1). In the absence of $NaBH_4$, the $Fe_3O_4$@P(EGDMA-co-MAA)/Au catalyst showed no catalytic activity (entry 2, Table 1). As expected, increasing the temperature enhanced the catalytic activity (entries 3 and 4, Table 1). In Fig. 3a, the reaction rate constant ($k$) is compared under different temperatures with the use of 2.5 mol% of $Fe_3O_4$@P(EGDMA-co-MAA)/Au and 100 equiv. of $NaBH_4$. The highest catalytic efficiency (0.330 $min^{-1}$) was obtained at 35 °C. The amount of catalyst as well as the amount of $NaBH_4$ used during the reduction was also optimized (entries 5 and 6, Table 1). The reduction was completed in 45 s when $Fe_3O_4$@P(EGDMAco-MAA)/Au was used as the catalyst (5.0 mol% of catalyst, 300 equiv. of $NaBH_4$ per equiv. substrate) (Fig. 3b). $Fe_3O_4$@P(EGDMA-co-MAA)/Au microspheres with different loadings of Au (11 and 18 wt.%) were also used as catalysts, resulting in lower catalytic activity (entries 7 and 8, Table 1). The $Fe_3O_4$@P(EGDMA-co-MAA)/Au catalyst exhibited superior catalytic activity to that previously reported for Au–$CeO_2$ nanocomposites and hybrid Au nanoparticle-GO nanosheets based on comparison of the turnover frequency (TOF) value [67,68]. APTS-modified $Fe_3O_4$@P(EGDMA-co-MAA)/Au and $Fe_3O_4$@$SiO_2$/Au catalysts were synthesized and applied in this reaction as catalysts (Fig. 4a and b). Au NPs were immobilized on APTS-modified $Fe_3O_4$@P(EGDMA-co-MAA) and $Fe_3O_4$@$SiO_2$. However, catalysts with low metal loadings were obtained as compared with the $Fe_3O_4$@P(EGDMA-co-MAA)/Au catalyst. The $Fe_3O_4$@P(EGDMA-co-MAA)/Au

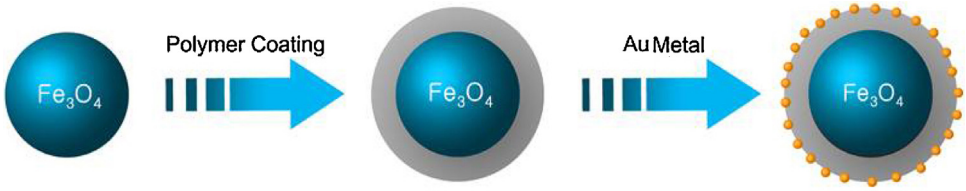


**Scheme 2.** An illustration of synthesis for $Fe_3O_4$@polymer/Au.

Please cite this article in press as: H. Woo, K.H. Park, Recent developments in hybrid iron oxide–noble metal nanocatalysts for organic reactions, Catal. Today (2016), http://dx.doi.org/10.1016/j.cattod.2016.01.030

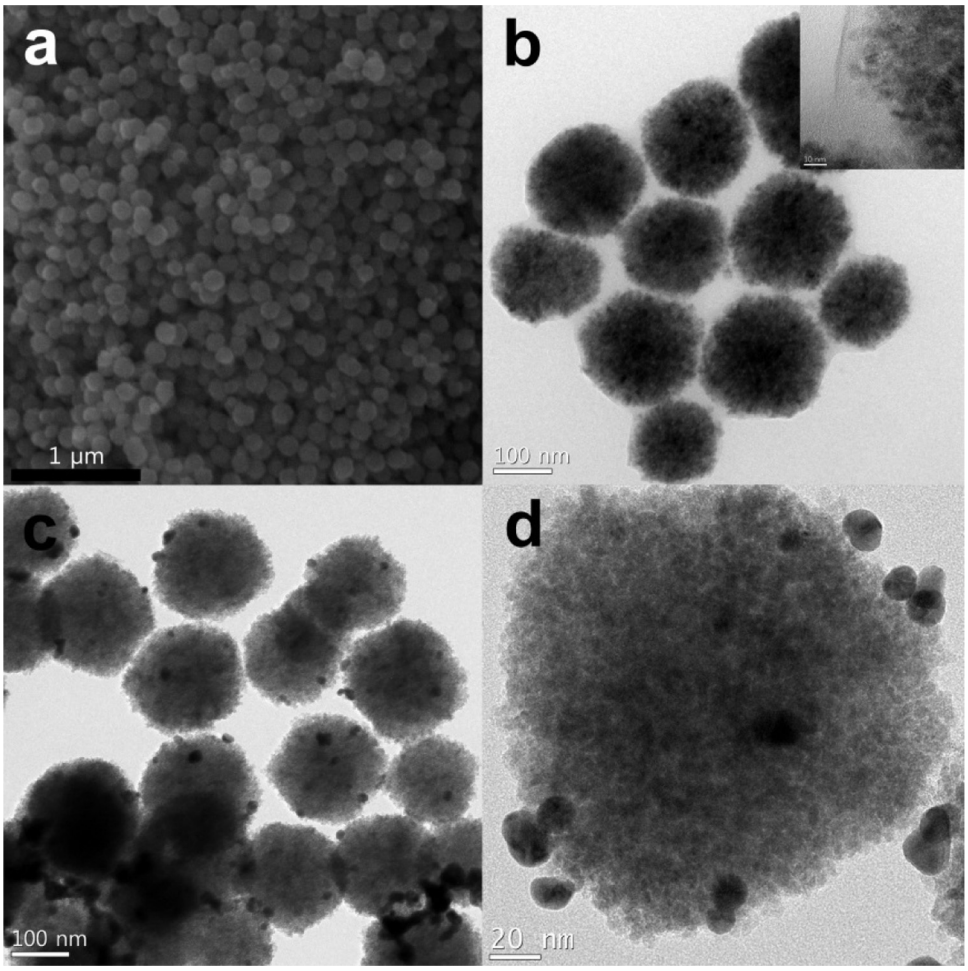


**Fig. 1.** (a) Scanning electron microscopy (SEM) image of $Fe_3O_4$ microspheres. (b) TEM images and magnified image of $Fe_3O_4$@P(EGDMA-co-MAA). Scale bar shows 10 nm (inset). (c) $Fe_3O_4$@P(EGDMA-co-MAA)/Au. (d) Magnified image of $Fe_3O_4$@P(EGDMA-co-MAA)/Au.

**Table 1**
Optimized reaction condition.

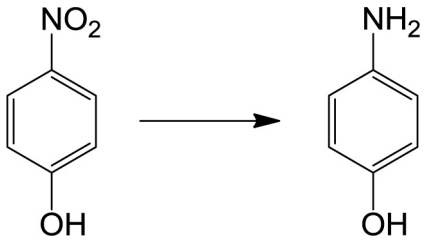


| Entry | Catalyst (mol%) | $NaBH_4$ (equiv.) | Time | TOF ($h^{-1}$) |
|---|---|---|---|---|
| 1 | $Fe_3O_4$@P(EGDMA-co-MAA) (2.5) | 300 | 2 h | No reaction |
| 2 | $Fe_3O_4$@P(EGDMA-co-MAA)/Au (2.5) | 0 | 2 h | No reaction |
| 3 | $Fe_3O_4$@P(EGDMA-co-MAA)/Au (2.5) | 100 | 25 min | 96 |
| 4 | $Fe_3O_4$@P(EGDMA-co-MAA)/Au (2.5) | 100 | 6 min | 600 |
| 5 | $Fe_3O_4$@P(EGDMA-co-MAA)/Au (2.5) | 300 | 4 min 38 s | 518 |
| 6 | $Fe_3O_4$@P(EGDMA-co-MAA)/Au (5.0) | 300 | 45 s | 1600 |
| 7 | $Fe_3O_4$@P(EGDMA-co-MAA)/Au (5.0, Au base: 11 wt.%) | 300 | 1 min 10 s | 1029 |
| 8 | $Fe_3O_4$@P(EGDMA-co-MAA)/Au (5.0, Au base: 18 wt.%) | 300 | 3 min | 400 |
| 9 | APTS-modified $Fe_3O_4$@P(EGDMA-co-MAA)/Au (2.5) | 300 | 2 h | 20 |
| 10 | APTS-modified $Fe_3O_4$@$SiO_2$/Au (2.5) | 300 | 2 h 15 min | 17.8 |

Reaction condition: 10 mL of $7.50 \times 10^{-4}$ M 4-nitrophenol, 0.25 mg of $Fe_3O_4$@P(EGDMA-co-MAA)/Au [Au base (15 wt.%): 2.5 mol%], 1.0 mL of 2.22 M $NaBH_4$ (300 equiv. to the substrate), 25 °C.

catalyst showed higher catalytic efficiency (0.354 $min^{-1}$) than the APTS-modified $Fe_3O_4$@P(EGDMA-co-MAA)/Au (0.0127 $min^{-1}$) and APTS-modified-$Fe_3O_4$@$SiO_2$/Au (0.00993 $min^{-1}$) (entries 5, 9 and 10, Table 1) congeners (Fig. 3c). In the synthesis of the $Fe_3O_4$@P(EGDMA-co-MAA)/Au catalyst, uniform Au NPs were immobilized onto $Fe_3O_4$@P(EGDMA-co-MAA) in situ without any treatment of the functional groups, resulting in high catalytic activity for reduction of 4-nitrophenol. Remarkably, after the

Please cite this article in press as: H. Woo, K.H. Park, Recent developments in hybrid iron oxide–noble metal nanocatalysts for organic reactions, Catal. Today (2016), http://dx.doi.org/10.1016/j.cattod.2016.01.030

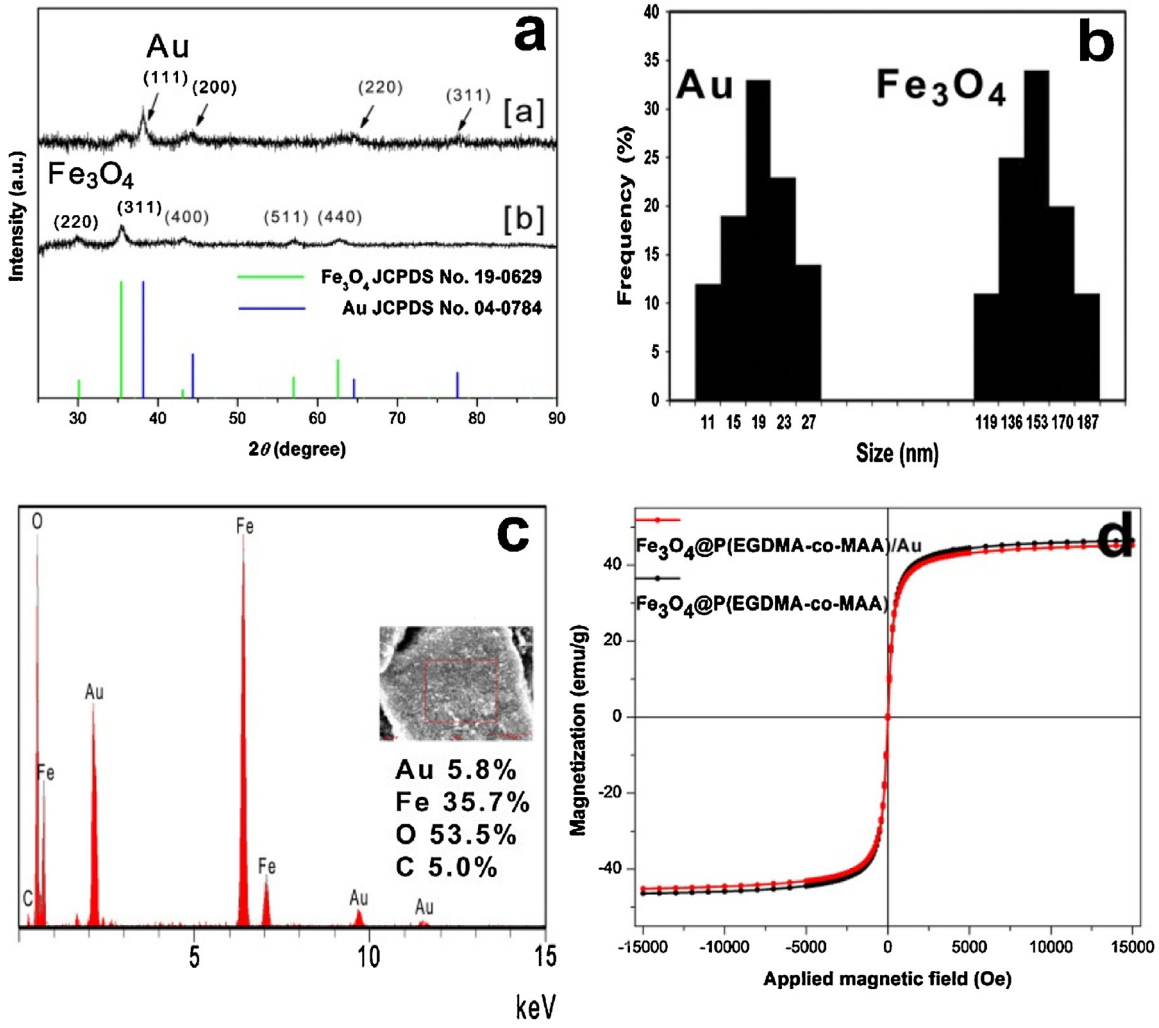


**Fig. 2.** (a) XRD patterns of $Fe_3O_4$@P(EGDMA-co-MAA)/Au [a] and $Fe_3O_4$ microspheres [b], (b) Size distribution diagrams of the Au NPs and $Fe_3O_4$ microspheres, (c) EDS spectrum of $Fe_3O_4$@P(EGDMA-co-MAA)/Au catalyst, (d) SQUID data.

reaction, the $Fe_3O_4$@P(EGDMA-co-MAA)/Au catalyst could be extracted from the reaction mixture with an external magnet and reused for four reaction cycles under the same reaction conditions (Fig. 3d).

## 3. Optimized dispersion and stability of $Fe_3O_4$/Pd catalysts [69]

To fabricate a suitable hybrid magnetic catalyst, it is quite necessary to develop techniques for controlling the dispersion of the catalysts in various solvents to apply them to functional materials. According to the classical Derjaguin–Landau–Verwey–Overbeek (DLVO) theory, the stability of particle dispersion is determined by the sum of the repulsive electrostatic forces and attractive van der Waals forces [70]. Thus, several approaches have been utilized for surface modification of NPs or microspheres to facilitate dispersion in organic solvents, and many organic capping agents have been used for enhancing the dispersion stability and solubility of IONPS [71–73]. $Fe_3O_4$ microspheres were synthesized by using different capping agents and the effect of the capping agents on the dispersion stability and catalytic activity of the $Fe_3O_4$/Pd composite for suzuki coupling reactions in water were evaluated (Scheme 3) [69].

The resulting $Fe_3O_4$ microspheres are shown in Fig. 5. All of the $Fe_3O_4$ microspheres were spherical with a rough surface. When $Na_3Cit$, polyethylene glycol (PEG) and polyvinylpyrrolidone (PVP) were used as capping agents, the respective average diameters of the $Fe_3O_4$ microspheres were 142, 150, and 153 nm. However, the average diameter increased to 175 nm in the absence of capping agents (Fig. 5d). Each type of $Fe_3O_4$ microsphere consisted of aggregates of small magnetite particles with a mean size of 3 nm, as observed via TEM (Fig. 6).

The TEM images show that Pd NPs with diameters of ca. 4 nm were immobilized onto each $Fe_3O_4$ microsphere by substituting the sodium cations with Pd ions in aqueous medium (Fig. 6) [61]. The size distribution plots of each Pd NP are shown in Fig. 6, demonstrating that the size of the Pd NPs was generally less than 5 nm. During the catalyst preparation, because the Pd NPs were immobilized onto $Fe_3O_4$ microspheres in aqueous solution, $Na_3Cit$-$Fe_3O_4$ and PEG-$Fe_3O_4$ could be well dispersed in the aqueous solution due to the hydrophilic functional groups of the capping agents, resulting in high monodispersity of the Pd NPs on the $Fe_3O_4$ microspheres (Fig. 6a and b). The $Fe_3O_4$ microspheres without capping agents also showed high dispersion in water because of the hydroxyl groups present on magnetite, which resulted in strong immobilization of the Pd NPs (Fig. 6c). The use of PVP as an organic capping agent

Please cite this article in press as: H. Woo, K.H. Park, Recent developments in hybrid iron oxide–noble metal nanocatalysts for organic reactions, Catal. Today (2016), http://dx.doi.org/10.1016/j.cattod.2016.01.030

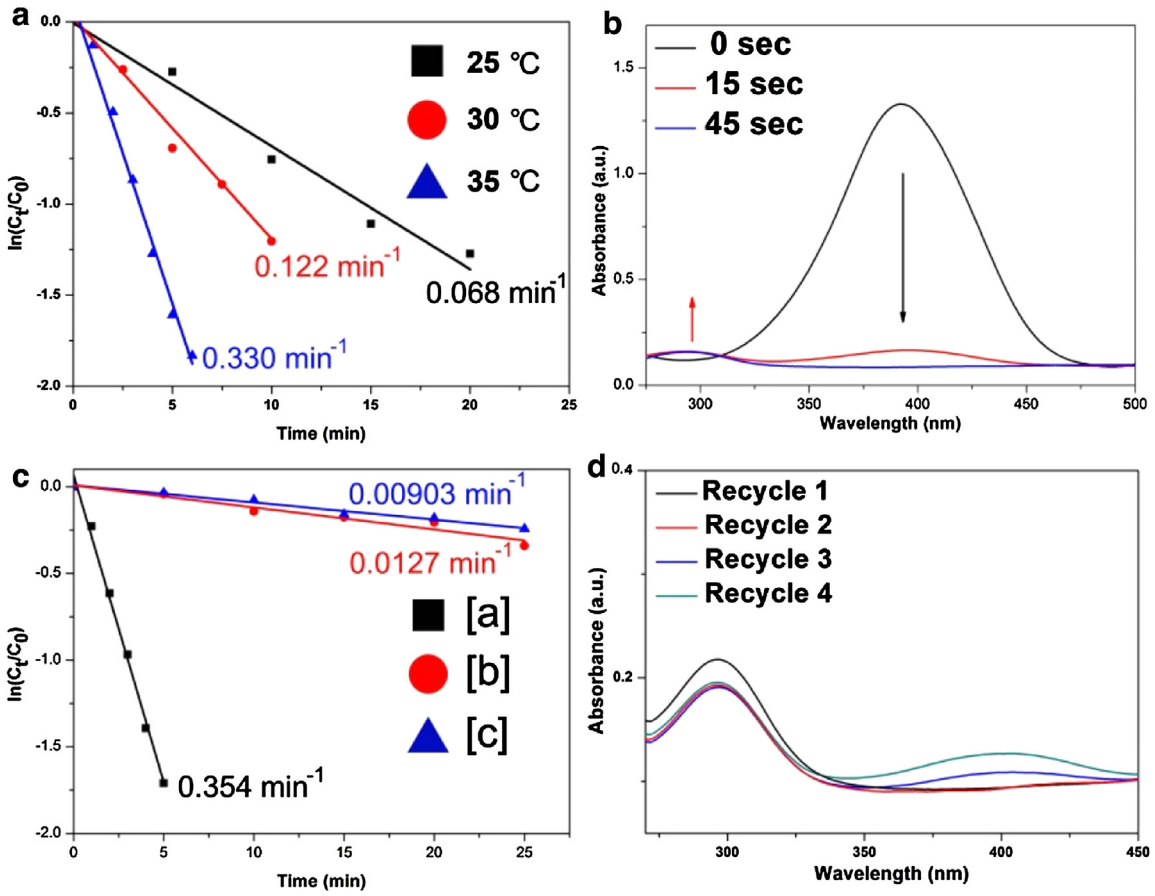


**Fig. 3.** (a) Plot of $\ln(C_t/C_0)$ versus time and the corresponding Arrhenius plot for the reduction of 4-nitrophenol over $Fe_3O_4$@P(EGDMA-co-MAA)/Au catalysts under different temperatures at 2.5 mol% of catalyst and 100 equiv. of $NaBH_4$. (b) Plot of $\ln(C_t/C_0)$ versus time for the reduction of 4-nitrophenol with different catalysts. All catalysts are used at the same molar ratio of 2.5 mol% of catalyst and 300 equiv. of $NaBH_4$ for the reaction at R.T. [a] $Fe_3O_4$@P(EGDMA-co-MAA)/Au [b] APTS-modified $Fe_3O_4$@P(EGDMA-co-MAA)/Au [c] APTS-modified-$Fe_3O_4$@$SiO_2$/Au. Time-dependent UV/vis absorption spectra for the reduction of 4-nitrophenol over hybrid $Fe_3O_4$@P(EGDMA-co-MAA)/Au catalyst in aqueous media at 298 K. (c) $Fe_3O_4$@P(EGDMA-co-MAA)/Au. (d) Recycle test.

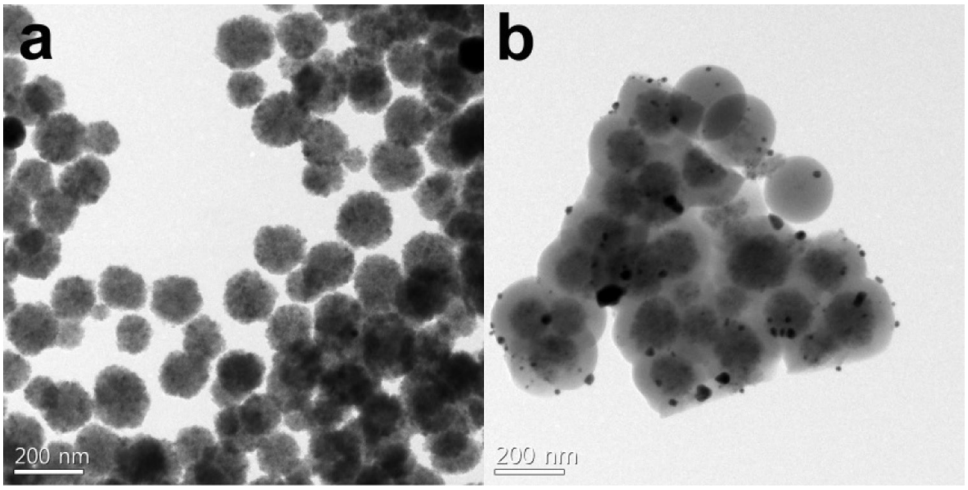


**Fig. 4.** TEM images of Au NPs on (a) APTS-modified $Fe_3O_4$@polymer and (b) $Fe_3O_4$@$SiO_2$ microspheres.

interrupted the dispersion of $Fe_3O_4$ in aqueous solution because of its hydrophobic nature as compared to the other capping agents, thereby making immobilization of the Pd NPs difficult (Fig. 6d).

XRD analysis (Fig. 7a) was used to identify the crystal phase of the respective $Fe_3O_4$/Pd microspheres. Specifically, the peaks were assigned to the (2 2 0), (3 1 1), (4 0 0), (4 2 2), and (5 1 1) reflections of the cubic spinel structure of $Fe_3O_4$ (JCPDS No. 19-0629) and the (1 1 1), (2 0 0), and (2 2 0) reflections of fcc Pd (JCPDS No. 46-1043). When the $Fe_3O_4$ microspheres were capped with $Na_3Cit$, the overall intensity of the XRD peaks of $Na_3Cit$-$Fe_3O_4$/Pd decreased. The SQUID data presented in Fig. 7b show the magnetic curves as a function of the applied field at 300 K. The saturation magnetization value of $Na_3Cit$-$Fe_3O_4$/Pd was 45.2 emu $g^{-1}$, which is similar to that of $Na_3Cit$-$Fe_3O_4$ (ca. 48.2 emu $g^{-1}$). The small decrease in

Please cite this article in press as: H. Woo, K.H. Park, Recent developments in hybrid iron oxide–noble metal nanocatalysts for organic reactions, Catal. Today (2016), http://dx.doi.org/10.1016/j.cattod.2016.01.030

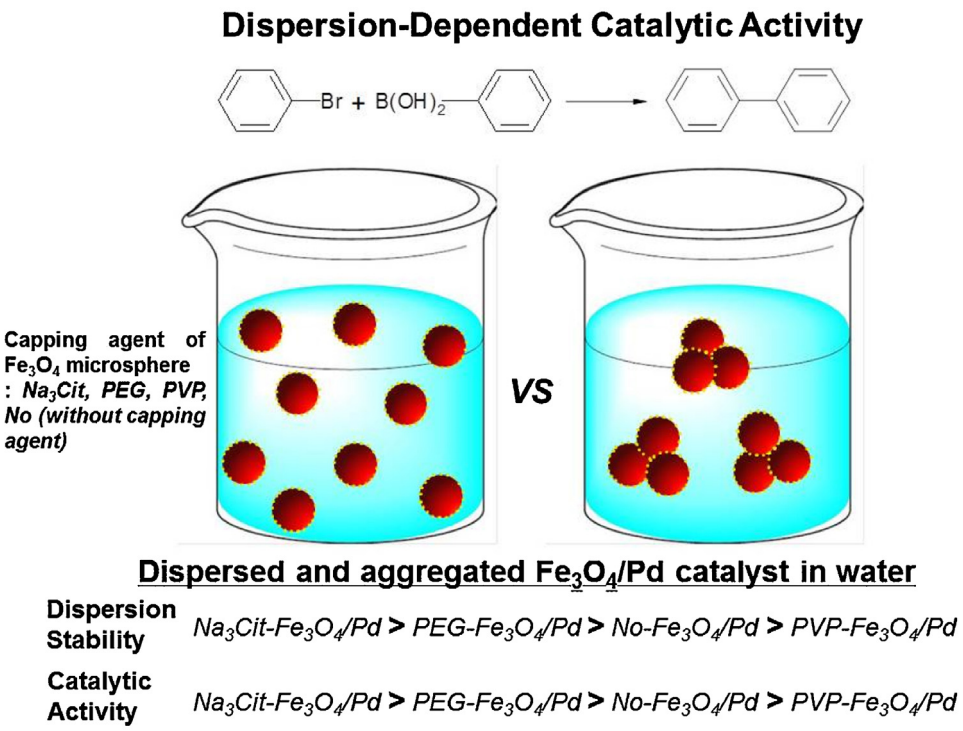


**Scheme 3.** Dispersion-dependent catalytic activity of $Fe_3O_4$/Pd catalysts in water for suzuki coupling reactions.

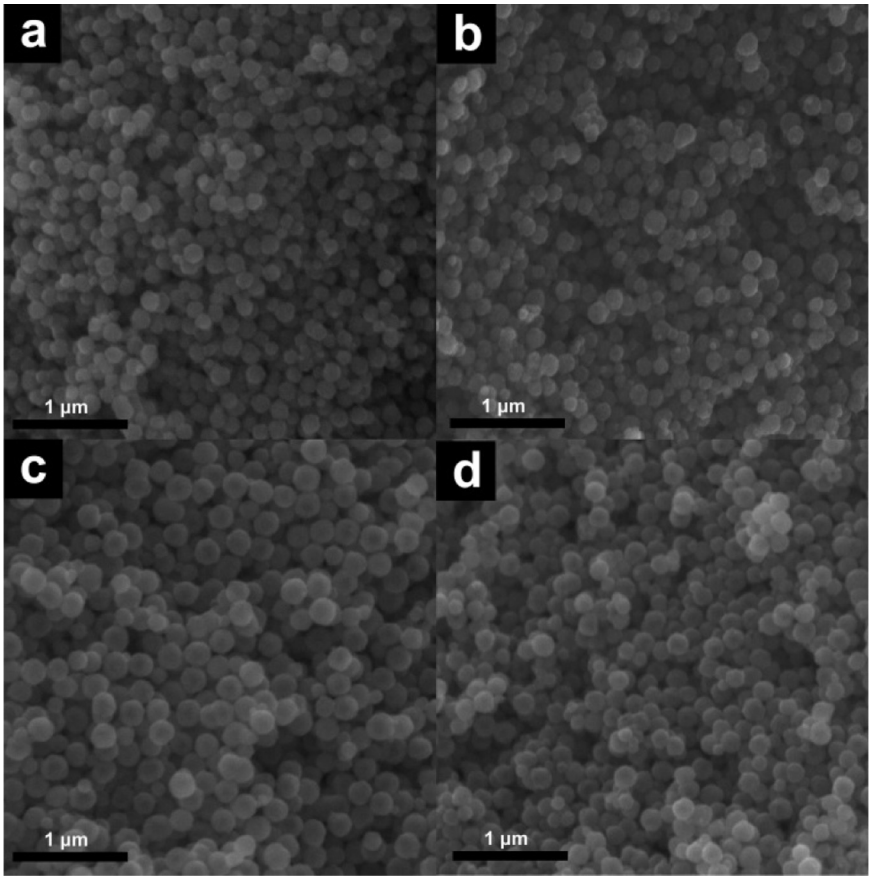


**Fig. 5.** SEM images of (a) $Na_3Cit$-$Fe_3O_4$, (b) PEG-$Fe_3O_4$, (c) No-$Fe_3O_4$ and (d) PVP-$Fe_3O_4$ microspheres.

Please cite this article in press as: H. Woo, K.H. Park, Recent developments in hybrid iron oxide–noble metal nanocatalysts for organic reactions, Catal. Today (2016), http://dx.doi.org/10.1016/j.cattod.2016.01.030

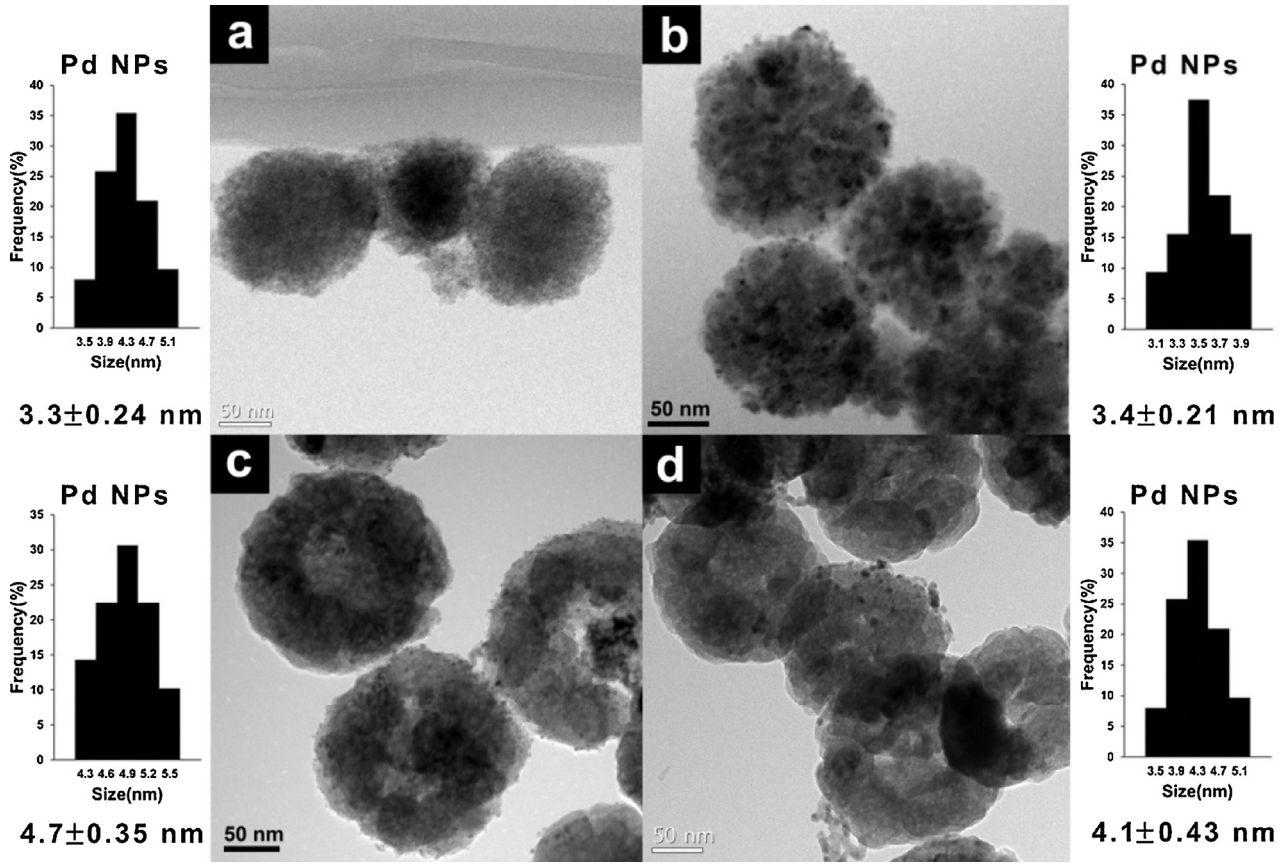


**Fig. 6.** TEM images of immobilized Pd NPs onto (a) $Na_3Cit$-$Fe_3O_4$, (b) PEG-$Fe_3O_4$, (c) No-$Fe_3O_4$ and (d) PVP-$Fe_3O_4$ microspheres. Size distribution graphs of each Pd NPs.

the saturated magnetization value of the $Na_3Cit$-$Fe_3O_4$/Pd microspheres compared to that of the $Na_3Cit$-$Fe_3O_4$ microspheres can be attributed to the slight increase in mass due to the immobilized Pd NPs on the surface of the $Fe_3O_4$ microspheres [74]. Moreover, the remanence and coercivity of the $Fe_3O_4$ microspheres were both close to zero, indicating superparamagnetism.

As mentioned above, the suzuki coupling reactions between bromobenzene and phenylboronic acid were used to investigate the catalytic activity of the hybrid catalysts; the results are summarized in Table 2. These results suggest that the bases, reaction time, and temperature utilized have dramatic effects on the yields of the cross-coupling product in this reaction. At 80 °C, 91% conversion was obtained in the mixture of DMF:$H_2O$ (4:1) (entry 1, Table 2). Interestingly, when the reaction temperature was decreased to 50 °C using only $H_2O$ as a solvent, high catalytic activity was achieved with the $Na_3Cit$-$Fe_3O_4$/Pd catalyst because this

**Table 2**
Optimized reaction conditions.

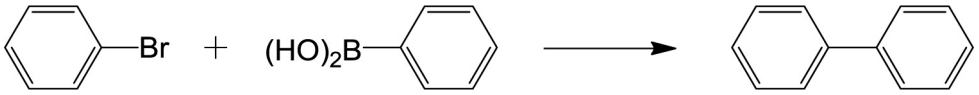


| Entry | Cat. (mol%) | Temp. (°C) | Time (h) | Base | Solvent | Conv. (%)[a] |
|---|---|---|---|---|---|---|
| 1 | 1 ($Na_3Cit$) | 80 | 5 | $K_2CO_3$ | DMF:$H_2O$ (4:1) | 91 |
| 2 | 1 ($Na_3Cit$) | 50 | 5 | $K_2CO_3$ | $H_2O$ | 97 |
| 3 | 0.1 ($Na_3Cit$) | 50 | 5 | $K_2CO_3$ | $H_2O$ | 65 |
| 4 | 0.05 ($Na_3Cit$) | 50 | 5 | $Cs_2CO_3$ | $H_2O$ | 89 |
| 5 | 0.05 ($Na_3Cit$) | 50 | 7 | $Cs_2CO_3$ | $H_2O$ | 98 |
| 6 | 0.05 ($Na_3Cit$) | 50 | 5 | CsOH | $H_2O$ | 66 |
| 7 | 0.05 ($Na_3Cit$) | 40 | 12 | $Cs_2CO_3$ | $H_2O$ | 48 |
| 8 | 0.05 ($Na_3Cit$) | 40 | 24 | $Cs_2CO_3$ | $H_2O$ | 94 |
| 9 | 0.1 ($Na_3Cit$) | 40 | 12 | $Cs_2CO_3$ | $H_2O$ | 76 |
| 10 | 0.05 ($Na_3Cit$) | 100 | 1 | $Cs_2CO_3$ | $H_2O$ | 80 |
| 11 | 0.05 ($Na_3Cit$) | 100 | 1.5 | $Cs_2CO_3$ | $H_2O$ | 98 |
| 12 | 0.05 ($Na_3Cit$) | 25 | 24 | $Cs_2CO_3$ | $H_2O$ | 13 |
| 13 | 0.05 (PEG) | 50 | 7 | $Cs_2CO_3$ | $H_2O$ | 89 |
| 14 | 0.05 (No) | 50 | 7 | $Cs_2CO_3$ | $H_2O$ | 57 |
| 15 | 0.05 (PVP) | 50 | 7 | $Cs_2CO_3$ | $H_2O$ | 37 |

Reaction conditions: $Na_3Cit$-$Fe_3O_4$/Pd catalyst (Pd base: 0.05 mol%), bromobenzene (0.5 mmol), phenylboronic acid (0.6 mmol), $Cs_2CO_3$ (1.0 mmol), $H_2O$ (3.0 mL) and 50 °C for 7 h.

[a] Determined by using GC-MS spectroscopy.

Please cite this article in press as: H. Woo, K.H. Park, Recent developments in hybrid iron oxide–noble metal nanocatalysts for organic reactions, Catal. Today (2016), http://dx.doi.org/10.1016/j.cattod.2016.01.030

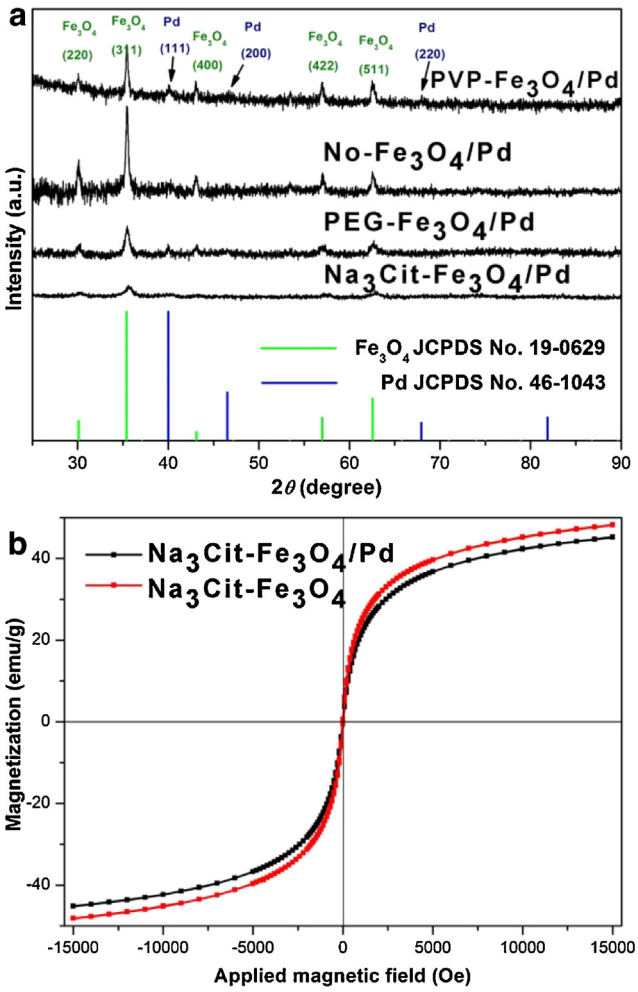


**Fig. 7.** (a) XRD pattern of each $Fe_3O_4$/Pd catalysts, (b) SQUID data.

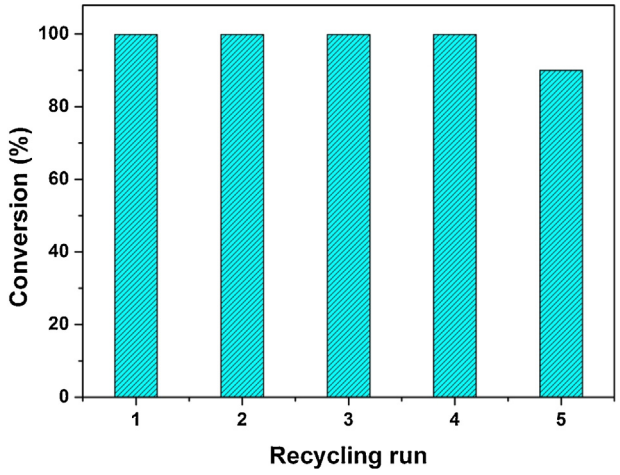


**Fig. 8.** Conversion during five recycling runs.

catalyst, capped by $Na_3Cit$, could be well dispersed in water (entry 2, Table 2). Preliminary screening for determining the most suitable base system for the catalyst revealed that $Cs_2CO_3$ could efficiently catalyze this reaction (entries 3, 4, and 6, Table 2). The optimum reaction conditions were found to be as follows: catalyst: $Na_3Cit$-$Fe_3O_4$/Pd (0.05 mol%); solvent: $H_2O$ (3.0 mL), temperature: 50 °C, reaction time: 7 h (entry 5, Table 2). At 40 °C, a reaction time of 24 h was necessary to obtain high yield (entries 7–9, Table 2). As expected, 98% conversion was achieved within 1.5 h at high temperature (100 °C) (entries 10 and 11, Table 2). The conversion decreased at room temperature, even though a reaction time of 24 h was used (entry 12, Table 2). The $Na_3Cit$-$Fe_3O_4$/Pd catalyst could be separated using an external magnet and could be recycled five times under the same reaction conditions (entry 11, Table 2) (Fig. 8).

Investigation of the dispersibility of nanomaterials in various solvents is crucial for environment-friendly applications [75]. Changes in the surface charge of the nanostructure in liquid media may produce drastic effects on the reactivity of nanomaterials [76–78]. Thus, surface modification of catalysts is considered a highly promising method for increasing the dispersion stability to effectively enhance the catalytic activity without aggregation. Here, we established a practical method for dispersing $Fe_3O_4$/Pd catalysts in aqueous solution and confirmed the catalytic activity by considering the differences in dispersibility. The stabilities of the $Fe_3O_4$/Pd catalysts coated with different capping agents of various hydrophilicities are shown in Fig. 9. Each $Fe_3O_4$/Pd catalyst was dispersed in water with a concentration of 1 mg/mL. The PVP-$Fe_3O_4$/Pd microspheres began to form agglomerates within 30 min because of the hydrophobicity of the PVP capping agent (Fig. 9a). No-$Fe_3O_4$/Pd was more stable in water than PVP-$Fe_3O_4$/Pd due to the presence of $OH^-$ anions on the surface of the bare $Fe_3O_4$ microspheres (Fig. 9b). Agglomeration of the PEG-$Fe_3O_4$/Pd and $Na_3Cit$-$Fe_3O_4$/Pd microspheres began within 5 and 7 days, respectively (Fig. 9c and d). Citrate and $OH^-$ anions on the $Fe_3O_4$ surface [61] enhanced the

Please cite this article in press as: H. Woo, K.H. Park, Recent developments in hybrid iron oxide–noble metal nanocatalysts for organic reactions, Catal. Today (2016), http://dx.doi.org/10.1016/j.cattod.2016.01.030

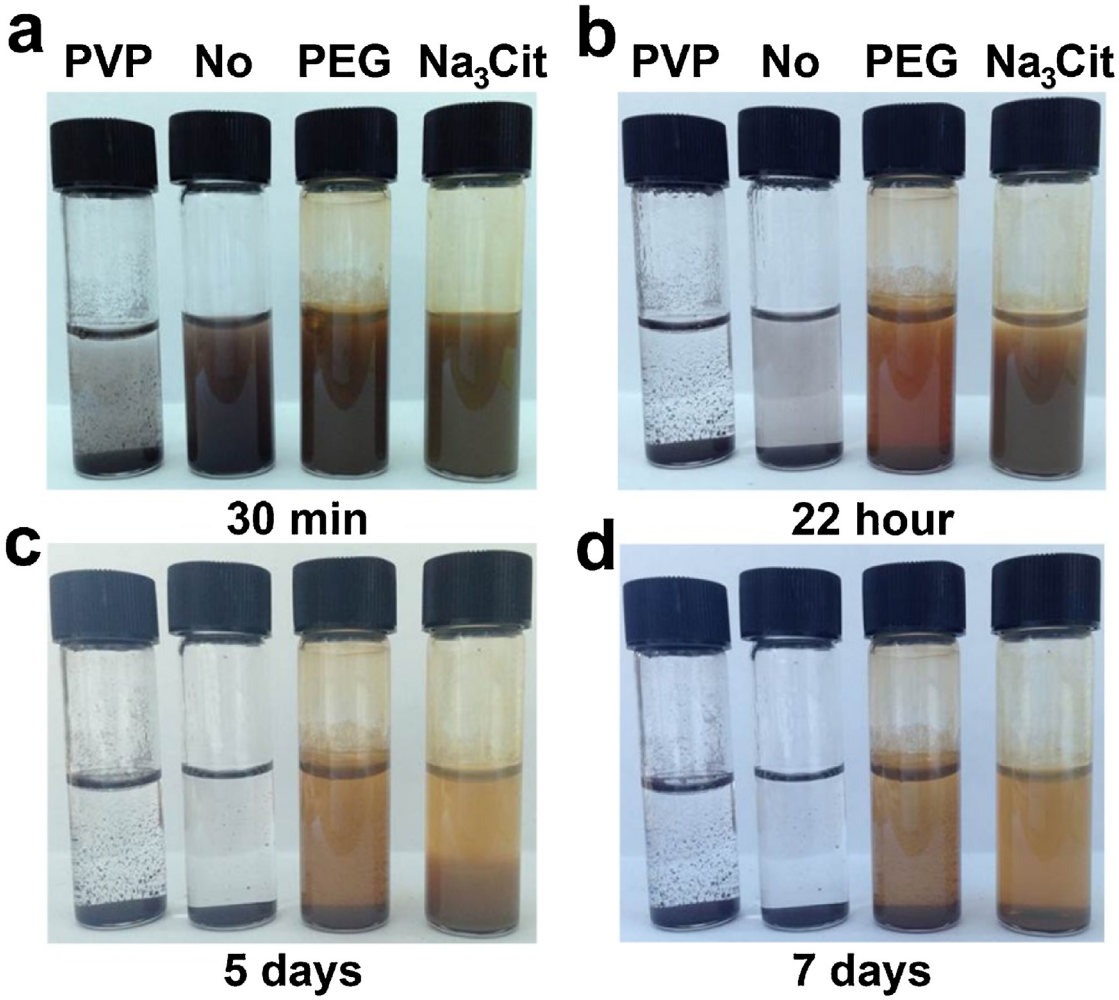


**Fig. 9.** Dispersion stability of $Fe_3O_4$/Pd catalysts after 30 min, 22 h, 5 days and 7 days, respectively. (PVP-$Fe_3O_4$/Pd, No-$Fe_3O_4$/Pd, PEG-$Fe_3O_4$/Pd and $Na_3Cit$-$Fe_3O_4$/Pd).

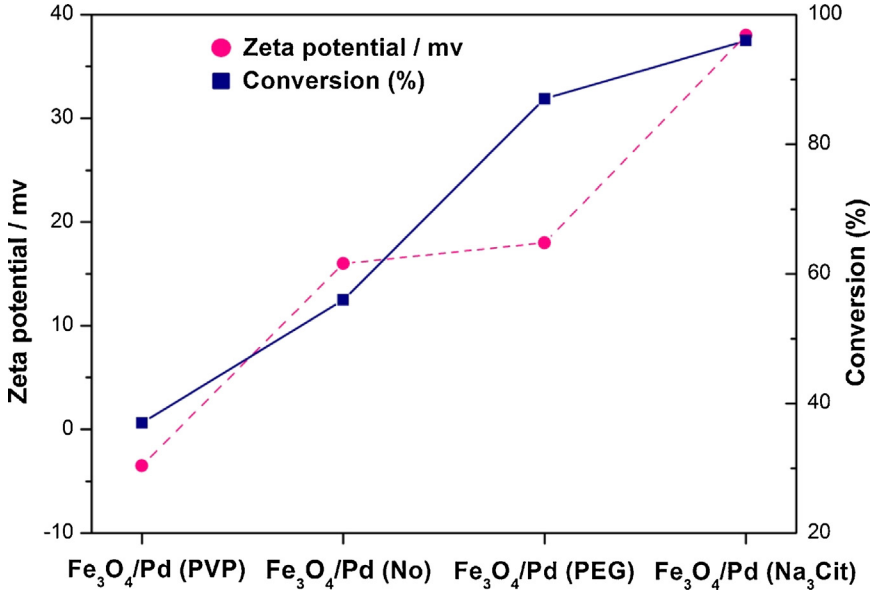


**Fig. 10.** Zeta potential and reaction conversion of $Fe_3O_4$/Pd microspheres capped by different capping agents at pH 7. Reaction conditions: $Fe_3O_4$/Pd catalysts (Pd base: 0.05 mol%), bromobenzene (0.5 mmol), phenylboronic acid (0.6 mmol), $Cs_2CO_3$ (1.0 mmol), $H_2O$ (3.0 mL) and 50 °C for 7 h.

Please cite this article in press as: H. Woo, K.H. Park, Recent developments in hybrid iron oxide–noble metal nanocatalysts for organic reactions, Catal. Today (2016), http://dx.doi.org/10.1016/j.cattod.2016.01.030

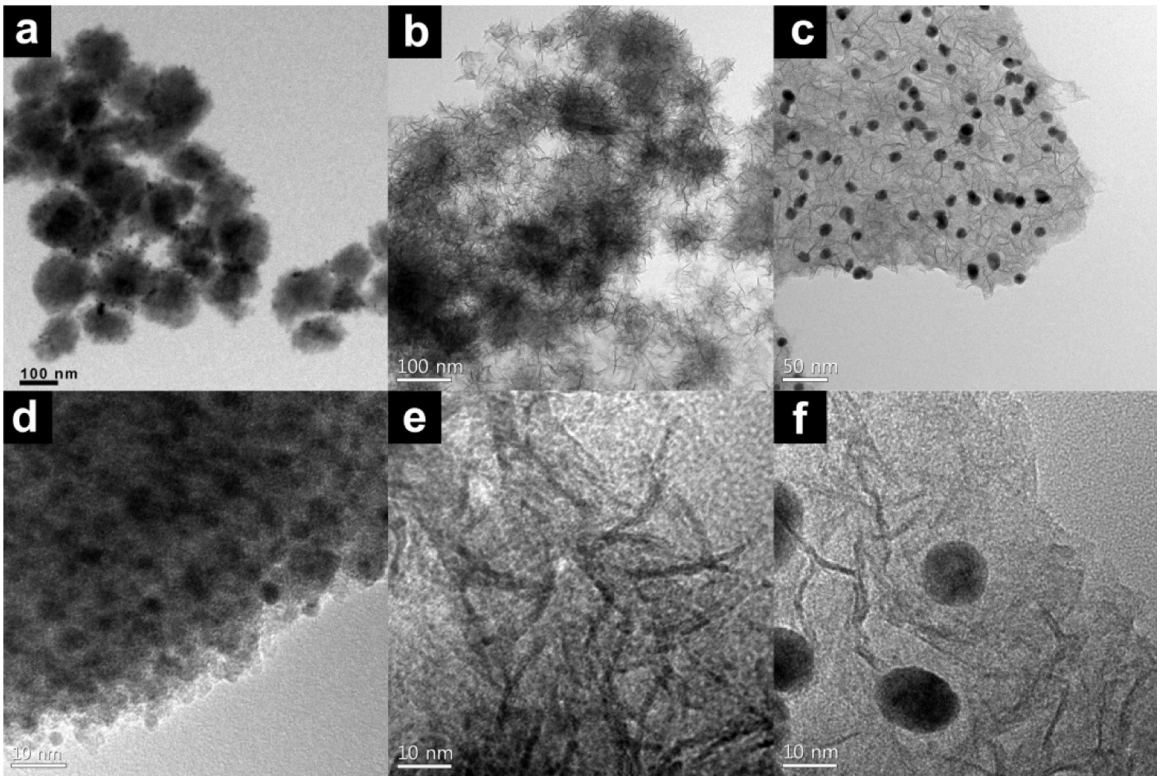


**Fig. 11.** TEM images of (a, d)Au/$Fe_3O_4$ microspheres, (b, e) $FeSO_4$·($H_2O$)-GO and (c, f) Au/$Fe_2O_3$-GO nanosheets.

**Table 3**
Surface areas, pore volumes and pore diameters of $FeSO_4$·($H_2O$)-GO, $Fe_2O_3$-GO and Au/$Fe_2O_3$-GO.

| Sample | BET surface area ($m^2\ g^{-1}$) | Langmuir surface area ($m^2\ g^{-1}$) | Pore volume ($cm^3\ g^{-1}$) | Pore diameter (nm) |
|---|---|---|---|---|
| $FeSO_4(H_2O)$-GO | 18.62 | 25.75 | 0.0342 | 11.5 |
| $Fe_2O_3$-GO | 213.0 | 291.8 | 0.233 | 4.48 |
| Au/$Fe_2O_3$-GO | 212.4 | 292.3 | 0.231 | 4.43 |

dispersion stability in water. The effect of the different capping agents on the zeta potential at pH 7 is shown in Fig. 10 to confirm the dispersion stability in water. On the basis of the literature, it was concluded that if the zeta potential of the particles is higher than 30 mV or lower than −30 mV, the dispersion is stable [79]. As the zeta potential increased, the conversion during the suzuki coupling reaction also increased (Fig. 10), indicating that the high dispersion stability of the catalysts in water, which precludes aggregation, leads to higher catalytic activity because of the increase in the available catalytically active sites. The $Na_3$Cit-$Fe_3O_4$/Pd catalyst had the highest zeta potential (38.3 mV) and gave rise to the greatest product conversion (98%) (Fig. 10). Because of the good dispersion stability of the developed $Na_3$Cit-$Fe_3O_4$/Pd catalyst in water, this catalyst showed higher catalytic activity than previously reported $Fe_3O_4$-supported Pd nanocatalysts [80–82] and has an environmentally positive impact and good overall industrial applicability.

## 4. Au NPs supported on $Fe_2O_3$-GO hybrid nanosheets [83]

Noble metal NPs with metal oxide supports and graphene oxide have been applied to organic reactions as catalysts [84–86]. For

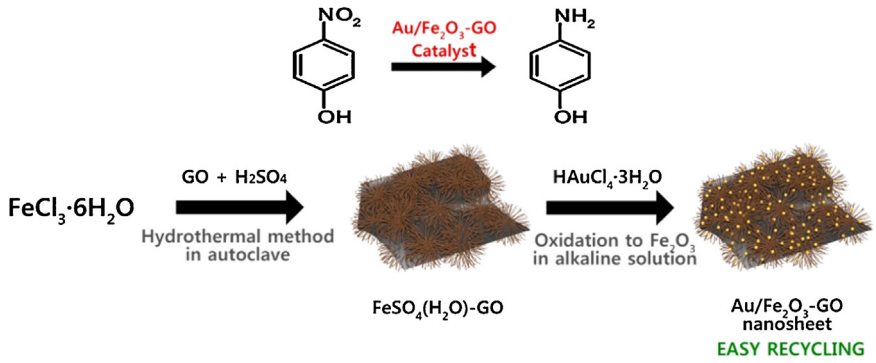


**Scheme 4.** Synthetic scheme of Au/$Fe_2O_3$-GO hybrid nanosheets.

Please cite this article in press as: H. Woo, K.H. Park, Recent developments in hybrid iron oxide–noble metal nanocatalysts for organic reactions, Catal. Today (2016), http://dx.doi.org/10.1016/j.cattod.2016.01.030

instance, Deng et al. [85] developed multi-functional mesoporous composite microspheres with well-designed nanostructures for an integrated catalyst system. Scheuermann et al. [86] reported Pd NPs on graphite oxide and their functionalized graphene derivatives with the aim of creating a hybrid catalytic system. Iron oxide and GO are important components used in a number of supports, since iron oxide can be separated from the reaction mixture with an external magnet and GO exhibits high electrical conductivity. Even though iron oxide supports show high recyclability, they are unstable in air and easily aggregate [87]. Moreover, although GO nanosheets offer the advantage of having surface functional groups as well as a large surface area [88], these nanosheets are not easily recycled by using an external magnet; therefore, it is essential to combine the advantages of iron oxide and GO. We synthesized $FeSO_4{\cdot}(H_2O)$-GO nanosheets by a one-pot method and subsequently immobilized Au NPs onto this support [83]. During the in situ immobilization of the Au NPs, $FeSO_4{\cdot}(H_2O)$ was transformed into $Fe_2O_3$ with consequent generation of superparamagnetic $Au/Fe_2O_3$-GO nanosheets. To the best of our knowledge, this is the first example of versatile synthesis of $Au/Fe_2O_3$-GO nanosheets. $Au/Fe_2O_3$-GO nanosheets were then used as a catalyst for the reduction of 4-nitrophenol in water, and high catalytic activity and recyclability were achieved.

The $Au/Fe_2O_3$-GO nanosheets were synthesized from $FeCl_3{\cdot}6H_2O$ via two steps (Scheme 4). $FeSO_4{\cdot}(H_2O)$-GO nanosheets were prepared by an in situ hydrothermal method [89]. A gold precursor was subsequently injected to yield $Au/Fe_2O_3$-GO nanosheets. GO nanosheets were used as the precursor to prepare $FeSO_4{\cdot}(H_2O)$-GO nanocomposites, which were synthesized from natural graphite powders by a modified Hummer's method [90]. For comparison, $Au/Fe_3O_4$ microspheres were also synthesized.

The TEM images show the morphology of the $Au/Fe_3O_4$ microspheres, $FeSO_4{\cdot}(H_2O)$-GO and $Au/Fe_2O_3$-GO nanosheets (Fig. 11). No pretreatment procedures such as coating polymers or $SiO_2$ onto $Fe_3O_4$ were required prior to immobilization of the Au NPs onto the $Fe_3O_4$ microspheres. In fact, the Au NPs were easily immobilized on the surface of $Fe_3O_4$ in situ via interaction of the carboxyl groups of $Na_3Cit$ with Au (Fig. 11a and d) [61]. The XRD pattern of the $Au/Fe_3O_4$ microspheres could be indexed to the cubic spinel structure of $Fe_3O_4$ (JCPDS No. 19-0629) and the fcc structure of Au (JCPDS No. 04-0784) (Fig. 12).

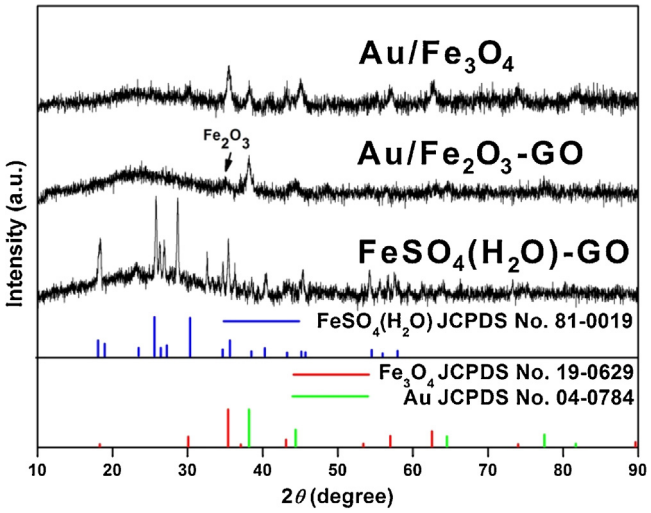


**Fig. 12.** XRD graphs of $FeSO_4{\cdot}(H_2O)$-GO, $Au/Fe_2O_3$-GO and $Au/Fe_3O_4$.

TEM images of the $FeSO_4{\cdot}(H_2O)$-GO nanocomposites are shown in Fig. 11b and e. The XRD pattern shown in Fig. 12 shows anorthic $FeSO_4{\cdot}(H_2O)$-GO reflections (JCPDS No. 81-0019). Elemental analysis of $FeSO_4{\cdot}(H_2O)$-GO using X-ray photoelectron spectroscopy (XPS) showed the $Fe^{2+}$ $2p_{3/2}$ peak of $FeSO_4{\cdot}(H_2O)$ at 710.9 eV; the binding energies of the doublet for $S^{6+}$ $2p_{1/2}$ (168.1 eV) and $S^{6+}$ $2p_{3/2}$ (168.6 eV) are shown in Fig. 13 and are consistent with the previously reported data for $FeSO_4{\cdot}(H_2O)$ (Fig. 13a and c) [91]. The binding energy of the C–C peak is assigned as 284.3 eV and shifts of +1.6 and +3.3 eV are typically assigned to the C—OH and C═O functional groups, respectively (Fig. 13b) [92].

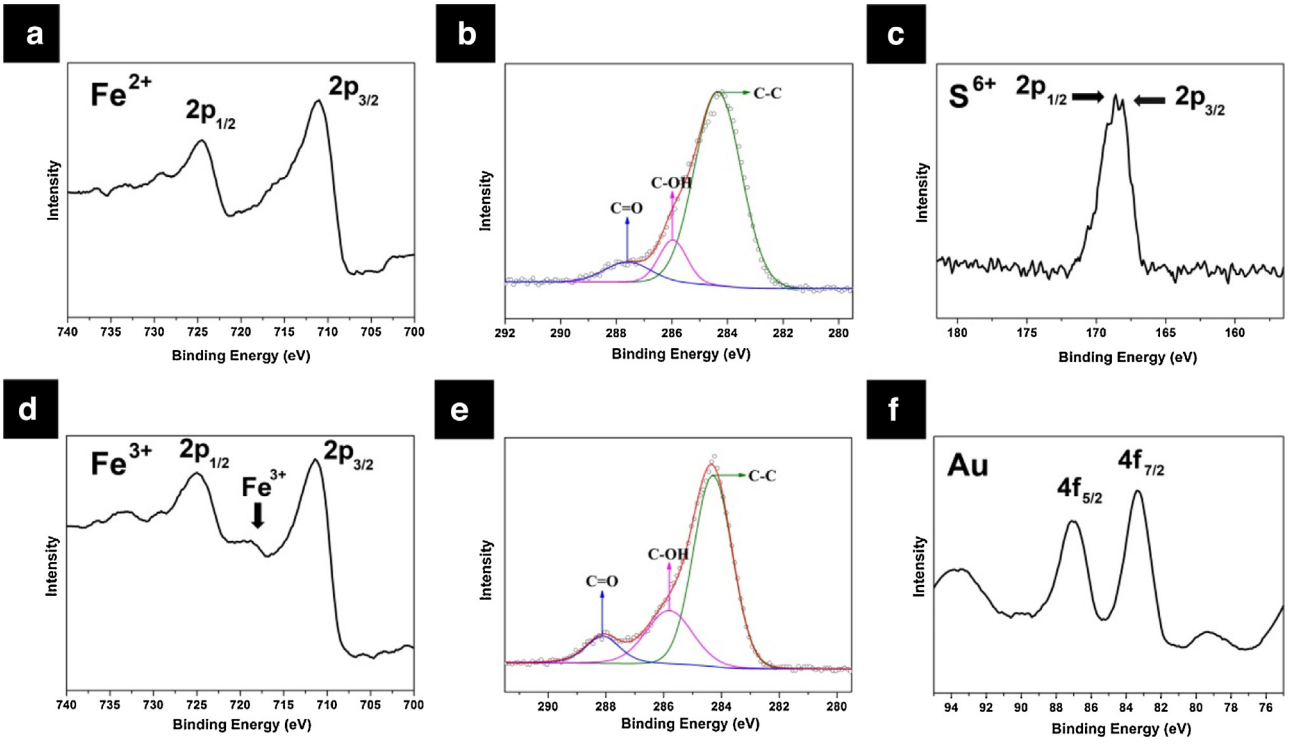


**Fig. 13.** The XPS spectra of $Fe^{2+}$, C and $S^{6+}$ of $FeSO_4{\cdot}(H_2O)$-GO (a–c) and $Fe^{3+}$, C and Au of $Au/Fe_2O_3$-GO (d–f).

Please cite this article in press as: H. Woo, K.H. Park, Recent developments in hybrid iron oxide–noble metal nanocatalysts for organic reactions, Catal. Today (2016), http://dx.doi.org/10.1016/j.cattod.2016.01.030

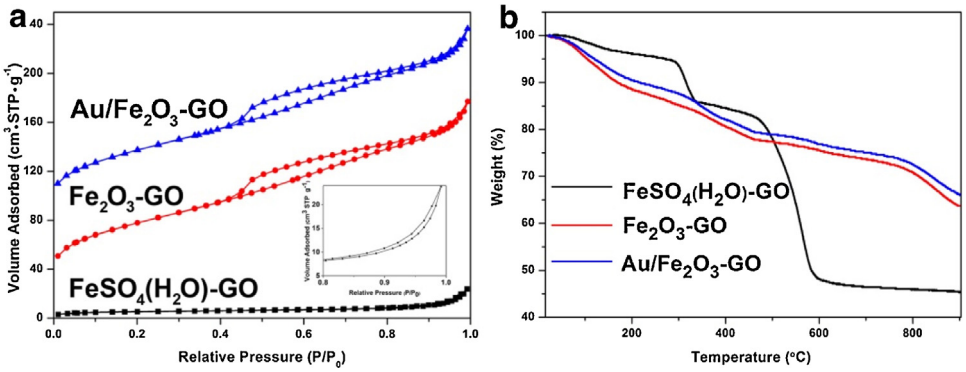


**Fig. 14.** (a) Nitrogen-adsorption/desorption isotherms and (b) TGA data of $FeSO_4{\cdot}(H_2O)$-GO, $Fe_2O_3$-GO and $Au/Fe_2O_3$-GO; for clarity, the isotherms of $Fe_2O_3$-GO and $Au/Fe_2O_3$-GO were shifted upwards by 50 and 110 $cm^3\ g^{-1}$, respectively.

In order to immobilize the Au NPs onto the $FeSO_4{\cdot}(H_2O)$-GO support, a method of exchanging sodium cations with noble metallic ions was applied [61]. Iron salts precipitate in alkaline aqueous solution [93], leading to the oxidation of $FeSO_4{\cdot}(H_2O)$ to $Fe_2O_3$ during immobilization of the Au NPs, resulting in formation of $Au/Fe_2O_3$-GO nanosheets. The TEM images show highly monodisperse Au NPs immobilized on the $Fe_2O_3$-GO nanosheets (Fig. 11c and f). Since it was difficult to assign the crystal phase of $Fe_2O_3$ due to the low intensity of the peaks in the XRD pattern (Fig. 12), we confirmed the $Fe_2O_3$ structure by using the XPS technique. In the case of high-spin iron, the Fe 2p peak is always split into two due to spin-orbit coupling (Fe $2p_{1/2}$, Fe $2p_{3/2}$). In the oxidized state (Fig. 13d), an additional satellite peak appears in-between the Fe $2p_{1/2}$ and Fe $2p_{3/2}$ components; in the case of $Fe_2O_3$, the satellite occurs 8 eV above the peak of the Fe $2p_{3/2}$ component [94]. The binding energy of C–C is also assigned as 284.3 eV and shifts of +1.5 and +3.8 eV are typically assigned to the C—OH and C=O functional groups, respectively (Fig. 13e) [92].

GO was further oxidized when the $Au/Fe_2O_3$-GO nanosheets were synthesized. The binding energies of the doublet for Au $4f_{7/2}$ (83.1 eV) and Au $4f_{5/2}$ (87.0 eV) shown in Fig. 13f are characteristic of $Au^0$ [95]. As a control experiment, $Fe_2O_3$-GO nanosheets were also synthesized without addition of $HAuCl_4{\cdot}3H_2O$. The $N_2$ adsorption/desorption isotherms (Fig. 14a) of $Fe_2O_3$-GO and the $Au/Fe_2O_3$-GO nanosheets were typical IV isotherms, indicating the presence of mesopores (4.4 nm) and a high surface area ($292\ m^2\ g^{-1}$). The textural characteristics of the corresponding samples are summarized in Table 3. Surprisingly, the surface area of $FeSO_4{\cdot}(H_2O)$-GO was less than $20\ m^2\ g^{-1}$ (Table 3). Thermogravimetric analysis (TGA) was also used to characterize the thermal stability of the three samples (Fig. 14). The TGA data showed different weight loss (%) trends for the $FeSO_4{\cdot}(H_2O)$-GO and $Fe_2O_3$-GO nanocomposites. It is postulated that the physical and chemical

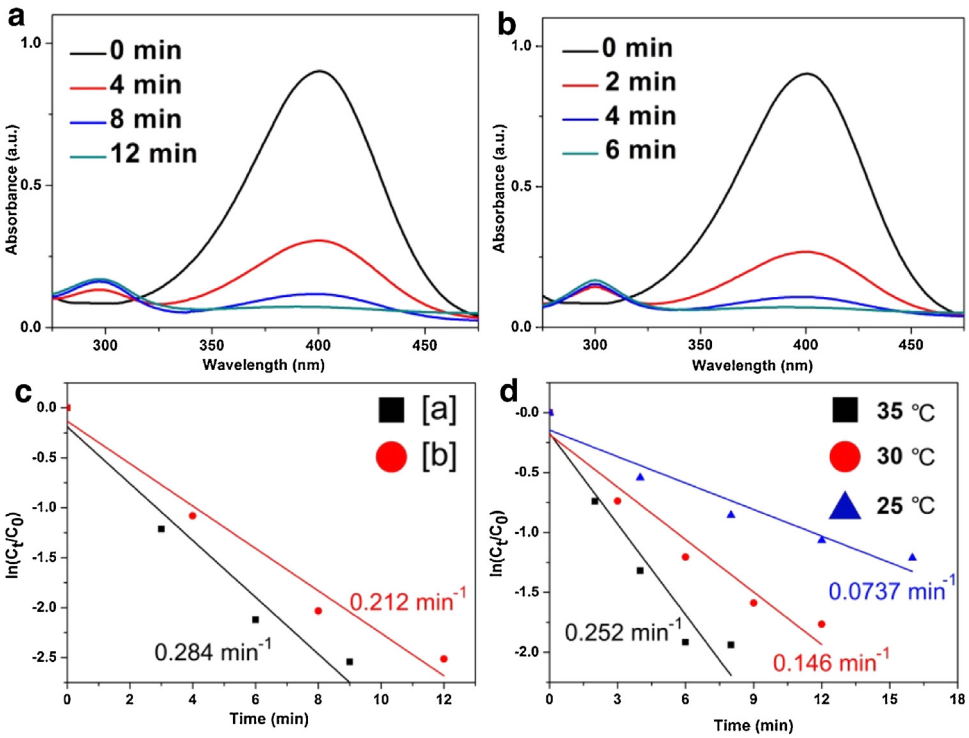


**Fig. 15.** Time-dependent UV/vis absorption spectra for the reduction of 4-nitrophenol over hybrid catalysts in aqueous media at 298 K. (a) $Au/Fe_2O_3$-GO (5.0 mol%). (b) $Au/Fe_3O_4$ (2.5 mol%). (c) Plot of $\ln(C_t/C_0)$ versus time with different catalysts. All catalysts are used at the same molar ratio of 5.0 mol% of catalyst and 100 equiv. of $NaBH_4$ for the reaction at R.T. [a] $Au/Fe_3O_4$ and [b] $Au/Fe_2O_3$-GO. (d) Plot of $\ln(C_t/C_0)$ versus time and the corresponding Arrhenius plot over $Au/Fe_2O_3$-GO catalysts under different temperatures at 5.0 mol% of catalyst and 50 equiv. of $NaBH_4$.

Please cite this article in press as: H. Woo, K.H. Park, Recent developments in hybrid iron oxide–noble metal nanocatalysts for organic reactions, Catal. Today (2016), http://dx.doi.org/10.1016/j.cattod.2016.01.030

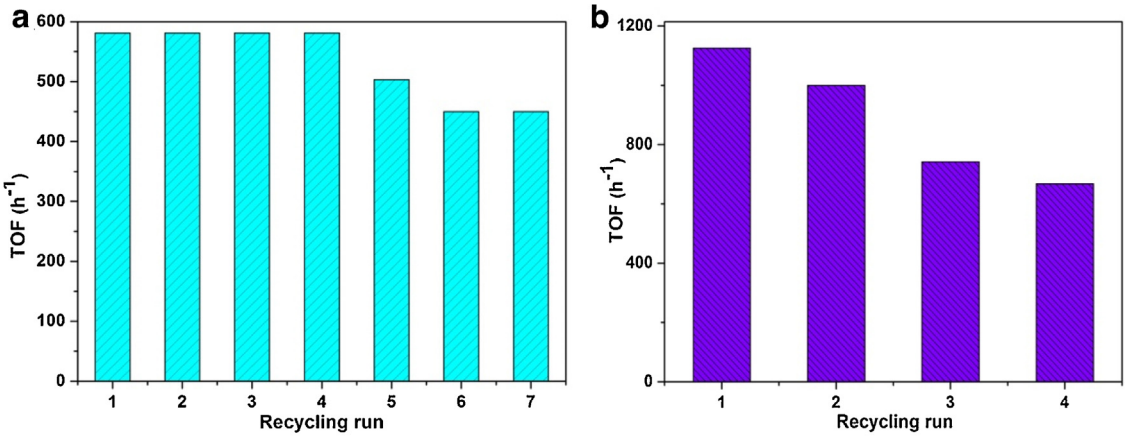


**Fig. 16.** (a) TOF during seven times recycling runs. Reaction condition: $Au/Fe_2O_3$-GO catalyst (Au base: 5.0 mol%), 200 equiv. of $NaBH_4$ and 35 °C. (b) TOF during four times recycling runs. Reaction condition: $Au/Fe_3O_4$ catalyst (Au base: 5.0 mol%), 200 equiv. of $NaBH_4$ and 35 °C.

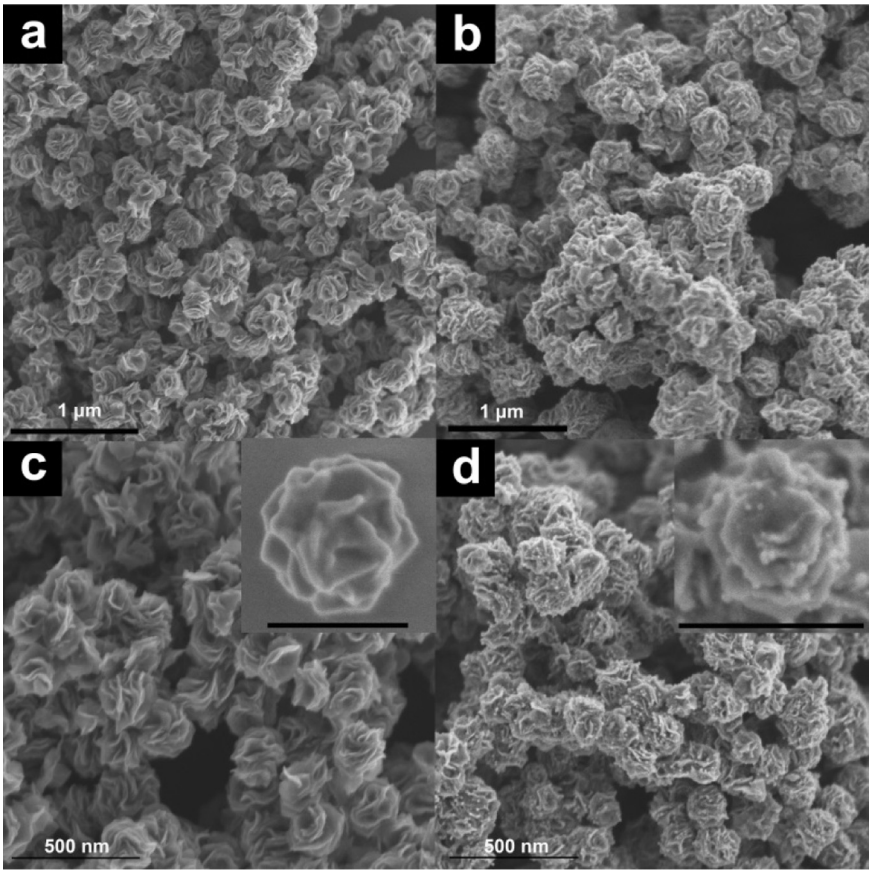


**Fig. 17.** SEM images of rose-like Pd-$Fe_3O_4$ (a, c) and Au/Pd-$Fe_3O_4$ (b, d) nanocomposites. The bars in the inset represent (c, d) 200 nm.

properties of $FeSO_4{\cdot}(H_2O)$-GO changed drastically in alkaline solution during immobilization of the Au NPs.

As shown in Fig. 15a and b, the UV/vis spectrum of the reaction mixture was monitored with time during the catalytic reduction of 4-nitrophenol. The reduction was complete in 12 min and 6 min when $Au/Fe_2O_3$-GO (5.0 mol%) and $Au/Fe_3O_4$ (2.5 mol%) were respectively used as the catalysts (100 equiv. of $NaBH_4$ per equiv. substrate at 298 K) (Fig. 15a and b).

As shown in Fig. 15c, the reaction constant ($k$) of the $Au/Fe_3O_4$ catalyst was higher (0.284 $min^{-1}$) than that achieved with the $Au/Fe_2O_3$-GO (0.212 $min^{-1}$) nanocomposites. The slightly higher catalytic activity of the $Au/Fe_3O_4$ catalyst is attributed to its better dispersion stability in water. Because $Fe_3O_4$ has many citrate groups and $OH^-$ anions, the dispersion stability of $Au/Fe_3O_4$ in water is enhanced. As shown in Fig. 15d, the reaction rate constant ($k$) was also compared with the use of different temperatures using 5.0 mol% of $Au/Fe_2O_3$-GO and 50 equiv. of $NaBH_4$. As expected, the highest catalytic efficiency (0.252 $min^{-1}$) was obtained at 35 °C. The $Au/Fe_3O_4$ and $Au/Fe_2O_3$-GO catalysts both exhibited superior catalytic activity relative to previously reported Au-$Fe_3O_4$ nanocomposites and Au-graphene nanosheets in terms of the reaction rate constant ($k$) [96,97]. It is believed that the electronic structures of the Au and metal oxide components are both modified by electron transfer across the interface of the Au-metal

Please cite this article in press as: H. Woo, K.H. Park, Recent developments in hybrid iron oxide–noble metal nanocatalysts for organic reactions, Catal. Today (2016), http://dx.doi.org/10.1016/j.cattod.2016.01.030

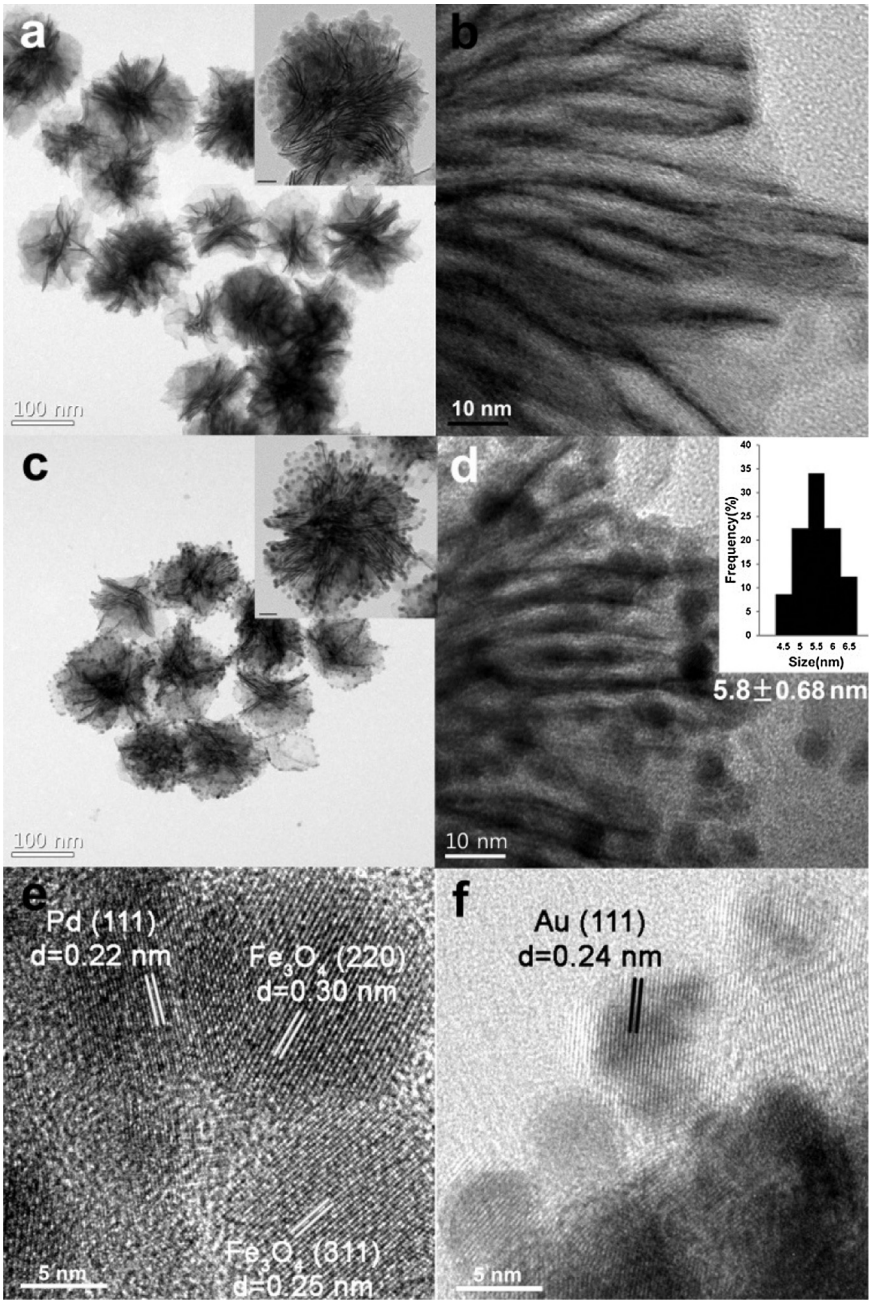


**Fig. 18.** TEM images of Pd–$Fe_3O_4$ (a, b) and Au/Pd–$Fe_3O_4$ (c, d). Au size distribution graph (d). HR-TEM images of Pd-$Fe_3O_4$ (e) and Au/Pd-$Fe_3O_4$ (f). The bars in the inset represent (a, c) 20 nm.

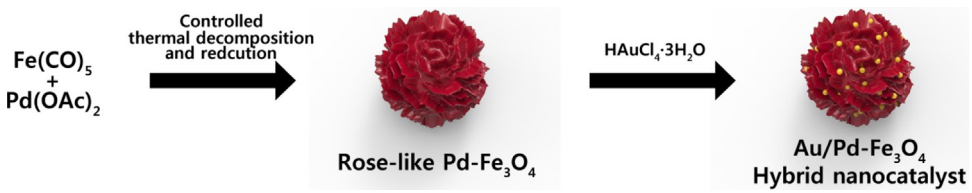


**Scheme 5.** Synthetic scheme of Au/Pd–$Fe_3O_4$ nanocomposites.

oxide hybrid NPs, giving rise to oxygen vacancies on the interfacial metal oxide that act as active sites for oxygen absorption and activation [98,99]. Thus, the hybrid NPs are catalytically more active than each individual component for the reduction of 4-nitrophenol. Remarkably, after the reaction, the Au/$Fe_2O_3$-GO catalyst could be recovered from the reaction mixture with an external magnet and reused seven times with only slight loss of catalytic activity (Fig. 16a). Even though the Au/$Fe_3O_4$ catalyst showed higher catalytic activity than the Au/$Fe_2O_3$-GO catalyst, the reusability of the Au/$Fe_3O_4$ catalyst declined drastically within four uses (Fig. 16b).

Please cite this article in press as: H. Woo, K.H. Park, Recent developments in hybrid iron oxide–noble metal nanocatalysts for organic reactions, Catal. Today (2016), http://dx.doi.org/10.1016/j.cattod.2016.01.030

## 5. Rose-like Pd–$Fe_3O_4$ hybrid nanocomposite supported Au nanocatalysts [100]

Numerous strategies have been developed for the design of new hybrid nanostructures with defined multicomponents by controlling the size and shape of these species through solution-growth fabrication [101–103]. Among the developed species, various multimetallic NPs have been reported by Mao et al. [104] and Mazumder et al. [105]. Mao et al. [104] reported a simple chemical synthetic route for producing FePt–Au hybrid nanostructures as catalysts for oxygen reduction reactions. Mazumder et al. [105] presented a unique approach for synthesizing core/shell-structured Pd/FePt NPs. Recently, they reported the one-pot synthesis of urchin-like FePd–$Fe_3O_4$ via controlled thermal decomposition of $Fe(CO)_5$ and reduction of $Pd(acac)_2$ [106]. We reported the facile synthesis of rose-like Pd–$Fe_3O_4$ nanocomposites, followed by immobilization of Au NPs onto these Pd–$Fe_3O_4$ supports (Scheme 5) [100]. These hybrid Au/Pd–$Fe_3O_4$ nanostructures showed high catalytic activity for the tandem synthesis of 2-phenylindoles and demonstrated magnetic recyclability.

The rose-like Pd–$Fe_3O_4$ nanocomposites were synthesized by facile decomposition of $Fe(CO)_5$ and reduction of $Pd(OAc)_2$ in oleylamine and 1-octadecene. The products were analyzed by inductively coupled plasma atomic emission spectroscopy (ICP-AES). Under the described synthesis conditions, the as-synthesized individual hybrid nanosheets, containing Pd and $Fe_3O_4$, formed three-dimensional rose-like Pd–$Fe_3O_4$ nanocomposites. The Fe/Pd ratios of the composites synthesized at 160 °C were controlled to 64:36–80:20 by increasing the amount of $Fe(CO)_5$ from 0.15 to 0.45 mL.

Fig. 17 shows SEM images of the rose-like Pd–$Fe_3O_4$ and Au/Pd–$Fe_3O_4$ hybrid nanocomposites with a well-distributed average diameter of 213 nm (Pd–$Fe_3O_4$). Au NPs were uniformly immobilized onto the Pd-$Fe_3O_4$ supports (Fig. 17b and d). The TEM images show Pd–$Fe_3O_4$ nanocomposites with an overall Fe/Pd ratio of 64:36 (Fig. 18a and b). The Au NPs immobilized on the Pd–$Fe_3O_4$ nanocomposites are shown in Fig. 18c and d. The immobilized Au NPs, with an average diameter of 5.8 nm, were spherical and highly monodisperse (Fig. 18d). The HR-TEM image of a representative Pd–$Fe_3O_4$ nanocomposite (Fig. 18e) shows that the Pd and $Fe_3O_4$ structures have well-defined and uniformly spaced lattice fringes with a measured fringe distance of 0.22 nm for the Pd (1 1 1) plane and 0.30 nm for the $Fe_3O_4$ (2 2 0) plane, corresponding to the fcc Pd and $Fe_3O_4$ structures, respectively. The Au NPs also have uniformly spaced lattice fringes, with a measured fringe distance of 0.24 nm, corresponding to the (1 1 1) interplanar spacing in the fcc Au structure (Fig. 18f).

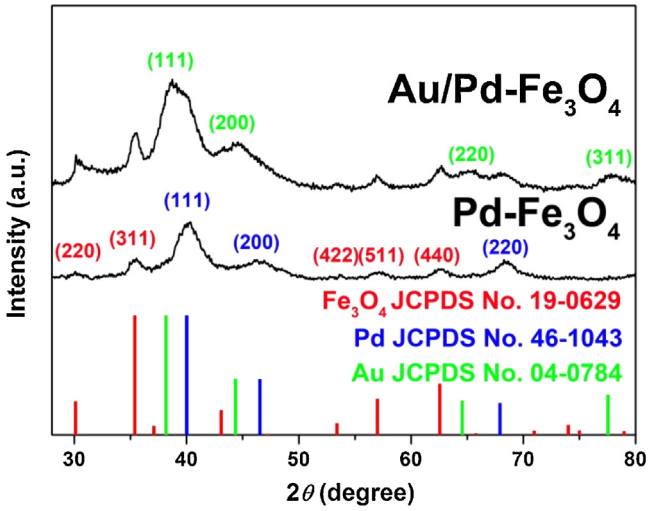


**Fig. 19.** XRD patterns of Pd–$Fe_3O_4$ and Au/Pd–$Fe_3O_4$.

The 3D flower-like structures are highly advantageous for use in sensors, lithium ion batteries, and photocatalysis because of their large specific surface area [107]. Brunauer–Emmett–Teller (BET) surface area analysis showed the surface area of the Pd–$Fe_3O_4$ nanocomposites to be 23.79 $m^2 g^{-1}$, which is much higher than that of the previously reported hollow and solid sphere-like $Fe_3O_4$ microspheres (12.27 and 5.43 $m^2 g^{-1}$, respectively) because of the individual Pd–$Fe_3O_4$ nanosheets [108].

The structures of the Au/Pd–$Fe_3O_4$ and Pd–$Fe_3O_4$ composites were further characterized by XRD. Fig. 19 shows the XRD patterns of the as-synthesized composites with overall element ratios of 7:77:16 (Au:Fe:Pd) and 64:36 (Fe:Pd). In the case of the Pd–$Fe_3O_4$ structure, all the peaks of the XRD pattern could be assigned to the (1 1 1), (2 0 0), and (2 2 0) lattice planes of the fcc Pd crystal structure (JPCDS No. 46-1043) and to the (2 2 0), (3 1 1), (4 2 2), (5 1 1), and (4 4 0) lattice planes of the cubic spinel structured $Fe_3O_4$ (JCPDS No. 19-0629). In the case of Au/Pd–$Fe_3O_4$, the reflections of the immobilized Au NPs were assigned to the (1 1 1), (2 0 0), (2 2 0), and (3 1 1) planes of the fcc Au crystal structure (JCPDS No. 04-0784). Specifically, the broadened diffraction peaks of the Au NPs are indicative of the small size of the crystal domains [109]. High-angle annular dark-field scanning TEM (HAADF-STEM) imaging and elemental

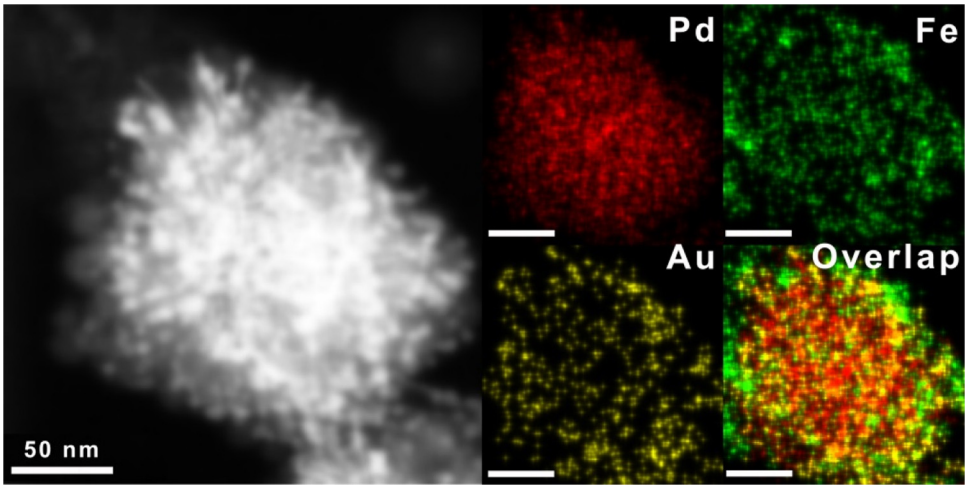


**Fig. 20.** HAADF-STEM image and elemental mapping of Au/Pd–$Fe_3O_4$. The bars in each element image represent 50 nm.

Please cite this article in press as: H. Woo, K.H. Park, Recent developments in hybrid iron oxide–noble metal nanocatalysts for organic reactions, Catal. Today (2016), http://dx.doi.org/10.1016/j.cattod.2016.01.030

**Table 4**
Tandem synthesis of 2-phenylindoles.

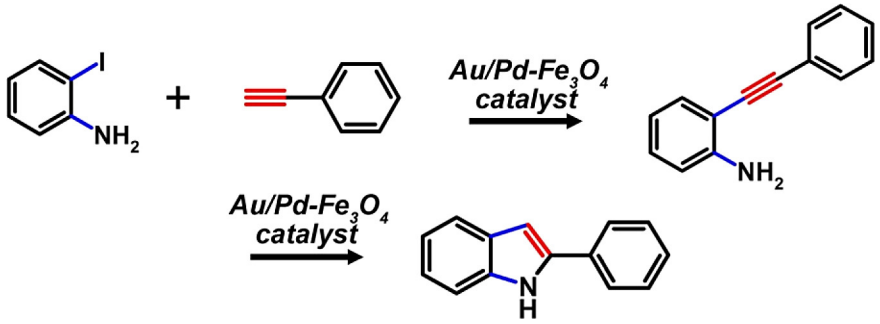


| Entry | Catalyst | Temp. (°C) | Time (h) | Base | Conversion (%)[a] |
|---|---|---|---|---|---|
| 1 | Pd–$Fe_3O_4$ | 120 | 18 | Piperidine | Trace[b] |
| 2 | Pd–$Fe_3O_4$ | 120 | 18 | Piperidine | 3[b] |
| 3 | Pd–$Fe_3O_4$ | 120 | 18 | Piperidine | 41 |
| 4 | Pd–$Fe_3O_4$ | 120 | 18 | LiOAc | 45 |
| 5 | Pd–$Fe_3O_4$ | 120 | 18 | CsOAc | 48 |
| 6 | Au/Pd–$Fe_3O_4$ | 120 | 18 | CsOAc | 57 |
| 7 | Au/Pd–$Fe_3O_4$ | 150 | 18 | CsOAc | 97 |
| 8 | Au/Pd–$Fe_3O_4$ | 150 | 9 | CsOAc | 97 |
| 9 | Au/Pd–$Fe_3O_4$ | 150 | 6 | CsOAc | 59 |
| 10 | Au/Pd–$Fe_3O_4$ | 150 | 9 | CsOAc | 38[c] |

Reaction condition: Au/Pd–$Fe_3O_4$ catalyst [Au base: 0.18 mol%, Pd base: 0.5 mol%], 2-iodoaniline (0.5 mmol), phenylacetylene (0.6 mmol), base (1.0 mmol), DMSO (2.5 mL).
[a] Determined by using GC-MS spectroscopy based on 2-iodoaniline.
[b] DMF and DMA was used as solvent, respectively.
[c] 0.09 mol% (Au base) of catalyst was used.

mapping also reveal that Au, Pd, and $Fe_3O_4$ are dispersed over the entire area of the composite, confirming the hybrid Au/Pd–$Fe_3O_4$ structure (Fig. 20).

To evaluate the catalytic activity of the Au/Pd–$Fe_3O_4$ catalyst, tandem synthesis of 2-phenylindoles from 2-iodoanilines with phenylacetylenes was performed as a model reaction under different conditions (Table 4). First, the effects of the solvents were examined in the presence of 0.5 mol% Pd–$Fe_3O_4$ catalyst at 120 °C using a reaction time of 18 h (entries 1–3, Table 4). The use of more polar solvents (DMSO) led to an increase in the conversion because of the superior solubility of the reactant and catalyst in the reaction medium. The influence of bases such as piperidine, LiOAc, and CsOAc was studied for the standard reaction (entries 3–5, Table 4).

The use of CsOAc led to good conversion (48%) compared to that achieved with piperidine and LiOAc. It was assumed according to the hard-soft acid and base theory that $Cs^+$ is the best Pearson acid for removal of iodide from the transient palladium NPs by maximization of the soft-soft interaction [110]. To date, dual-catalytic cross-coupling reactions with gold and palladium have continued to receive attention because of the novel reactivity that is unavailable in single-metal systems [111–113]. These dual-catalytic systems possess higher catalytic activities than single catalytic systems due to electron transfer across the interface and circumvent the formation of the stochiometric transmetalation byproducts that are common to cross-coupling reactions. Thus, the Au/Pd–$Fe_3O_4$ catalyst showed better catalytic activity than Pd–$Fe_3O_4$ since the Au NPs are highly efficient for activating phenylacetylene (entries 5 and 6, Table 4) [112]. As expected, 97% conversion was achieved at high temperature (150 °C) (entries 6 and 7, Table 4). The effects of the catalyst loading and reaction time were also evaluated. The conversion decreased (59 and 38%) when a short reaction time (6 h) and a lower catalyst loading (Au base: 0.09 mol%) were employed (entries 8–10, Table 4). The optimum reaction conditions were found to be as follows: Au/Pd–$Fe_3O_4$ (Au base: 0.18 mol%, Pd base: 0.5 mol%); solvent: DMSO (2.5 mL), temperature: 150 °C, reaction time: 9 h (entry 8, Table 4). Without the use of additives and ligands, the Au/Pd–$Fe_3O_4$ catalyst exhibited superior catalytic activity relative to previously reported copper and gold complexes and Au NPs in terms of the TOF value [114–116]. Catalytic activity was also compared with previous reported heterogeneous catalysts of our group (Fig. 21) [54,69,117–119]. Among them, Au/Pd–$Fe_3O_4$ exhibited the highest TOF value at the same condition and this could be attributed to dual-catalytic system between catalytic effective Pd–$Fe_3O_4$ support and Au NPs. The Pd–$Fe_3O_4$ support can also exhibit high catalytic activity since the individual Pd–$Fe_3O_4$ nanosheets with high surface area possess Pd° sites that can act as catalytically active sites. After the tandem reaction, the Au/Pd–$Fe_3O_4$ catalyst could be totally separated from the reaction medium with an external magnet owing to the superparamagnetism of the $Fe_3O_4$ particles [120]. The Au/Pd–$Fe_3O_4$ catalyst was recycled three times and its initial high activity (>99%) was still maintained without any loss

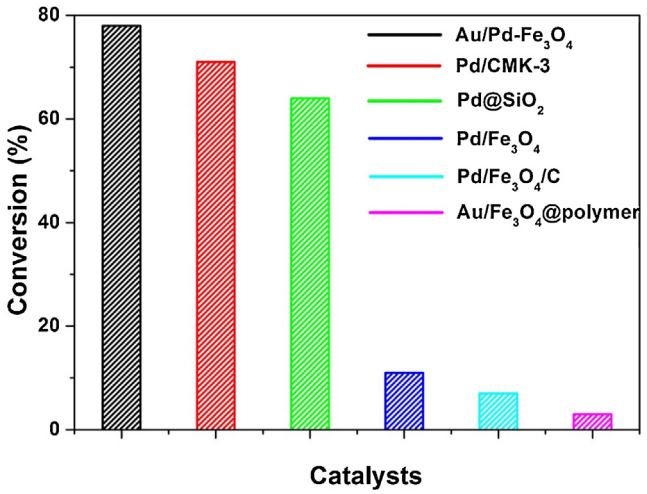


**Fig. 21.** Comparison of catalytic activity with previous reported heterogeneous catalysts in our group. Reaction condition: 2-iodoaniline (0.5 mmol), phenylacetylene (0.6 mmol), CsOAc (1.0 mmol), DMSO (2.5 mL), Catalyst (0.36 mol%), 150 °C, 4.5 h.

during the recycling process. Leaching of Pd and Au was analyzed by ICP-AES analysis of the filtered solution after the catalytic reaction, demonstrating a low content of Pd and Au of 79.8 and 80.9 ppm, respectively, in the solution.

## 6. Conclusion

The synthesis of hybrid iron oxide–noble metal nanocomposites was reviewed herein with focus on Au/$Fe_3O_4$@polymer, $Fe_3O_4$/Pd, Au/$Fe_2O_3$-GO, and Au/Pd–$Fe_3O_4$ composites. These hybrid nanocomposites act as efficient catalysts for reduction of 4-nitrophenol and in the suzuki coupling reaction and tandem synthesis of 2-phenylindoles. All of the hybrid catalysts exhibited better catalytic activity and recyclability than many previously catalysts. Hybrid noble metal NPs with supports are demonstrated to have great potential for tailoring of the activity, selectivity, and stability by judicious selection and exploitation of their numerous combinations.

## Acknowledgments

This research was supported by Basic Science Research Program through the National Research Foundation of Korea (NRF) funded by the Ministry of Science, ICT & Future Planning (NRF-2015R1D1A1A02060684 and NRF-2013R1A1A2012960) and GCRC-SOP (No.2011-0030013). K.H.P thanks to the TJ Park Junior Faculty Fellowship and LG Yonam Foundation.

## References

[1] S. Guo, L. Wang, S. Dong, E. Wang, J. Phys. Chem. C 112 (2008) 13510.
[2] V. Polshettiwar, R. Luque, A. Fihri, H. Zhu, M. Bouhrara, J.-M. Basset, Chem. Rev. 111 (2011) 3036.
[3] S. Chen, R. Si, E. Taylor, J. Janzen, J. Chen, J. Phys. Chem. C 116 (2012) 12969.
[4] S. Guo, S. Dong, E. Wang, ACS Nano 4 (2010) 547.
[5] D. Wen, S. Guo, Y. Wang, S. Dong, Langmuir 26 (2010) 11401.
[6] A. Fihri, M. Bouhrara, B. Nekoueishahraki, J.-M. Basset, V. Polshettiwar, Chem. Soc. Rev. 40 (2011) 5181.
[7] S. Shylesh, V. Schnemann, W.R. Thiel, Angew. Chem. Int. Ed. 49 (2010) 3428.
[8] C.-T. Hsieh, Y.-Y. Liu, D.-Y. Tzou, W.-Y. Chen, J. Phys. Chem. C 116 (2012) 26735.
[9] J.W. Ha, T.P.A. Ruberu, R. Han, B. Dong, J. Vela, N. Fang, J. Am. Chem. Soc. 136 (2014) 1398.
[10] D. Wang, Y. Li, J. Am. Chem. Soc. 132 (2010) 6280.
[11] X. Jin, L. Dang, J. Lohrman, B. Subramaniam, S. Ren, R.V. Chaudhari, ACS Nano 7 (2013) 1309.
[12] B. Dong, D.L. Miller, C.Y. Li, J. Phys. Chem. Lett. 3 (2012) 1346.
[13] S. Omar, R. Abu-Reziq, J. Phys. Chem. C 118 (2014) 30045.
[14] H. Hu, J.H. Xin, H. Hu, X. Wang, D. Miao, Y. Liu, J. Mater. Chem. A 3 (2015) 11157.
[15] S. Askari, R. Halladj, M.J. Azarhoosh, RSC Adv. 5 (2015) 52788.
[16] Y. Zheng, C. Chen, Y. Zhan, X. Lin, Q. Zheng, K. Wei, J. Zhu, J. Phys. Chem. C 112 (2008) 10773.
[17] R.K. Sharma, S. Sharma, S. Dutta, R. Zboril, M.B. Gawande, Green Chem. 17 (2015) 3207.
[18] H. Song, Acc. Chem. Res. 48 (2015) 491.
[19] L.-T. Guo, Y.-Y. Cai, J.-M. Ge, Y.-N. Zhang, L.-H. Gong, X.-H. Li, K.-X. Wang, Q.-Z. Ren, J. Su, J.-S. Chen, ACS Catal. 5 (2015) 388.
[20] S.M. Kim, S.J. Lee, S.H. Kim, S. Kwon, K.J. Yee, H. Song, G.A. Somorjai, J.Y. Park, Nano Lett. 13 (2013) 1352.
[21] J.-S. Choi, J.C. Park, H. Nah, S. Woo, J. Oh, K.M. Kim, G.J. Cheon, Y. Chang, J. Yoo, J. Cheon, Angew. Chem. Int. Ed. 47 (2008) 6259.
[22] P. Sun, H. Zhang, C. Liu, J. Fang, M. Wang, J. Chen, J. Zhang, C. Mao, S. Xu, Langmuir 26 (2010) 1278.
[23] H. Wang, D.W. Brandl, F. Le, P. Nordlander, N.J. Halas, Nano Lett. 6 (2006) 827.
[24] F.D. Angelis, M. Patrini, G. Das, I. Maksymov, M. Galli, L. Businaro, L.C. Andreani, E.D. Fabrizio, Nano Lett. 8 (2008) 2321.
[25] P. Viste, J. Plain, R. Jaffiol, A. Vial, P.M. Adam, P. Royer, ACS Nano 4 (2010) 759.
[26] S. Sun, C.B. Murray, D. Weller, L. Folks, A. Moser, Science 287 (2000) 1989–1992.
[27] M.M. Miller, G.A. Prinz, S.F. Cheng, S. Bounnak, Appl. Phys. Lett. 81 (2002) 2211.
[28] T.K. Jain, M.A. Morales, S.K. Sahoo, D.L. Leslie-Pelecky, V. Labhasetwar, Mol. Pharm. 2 (2005) 194.
[29] I. Chourpa, L. Douziech-Eyrolles, L. Ngaboni-Okassa, J.F. Fouquenet, S. Cohen-Jonathan, M. Souce, H. Marchais, P. Dubois, Analyst 130 (2005) 1395.
[30] J.W. Bulteí, Methods Mol. Med. 124 (2006) 419.
[31] M. Modo, J.W. Bulteí, Mol. Imaging 4 (2005) 143.
[32] C. Burtea, S. Laurent, A. Roch, L. Vander Elst, R.N. Muller, J. Inorg. Biochem. 99 (2005) 1135.
[33] S. Boutry, S. Laurent, L. Vander Elst, R.N. Muller, Contrast Med. Mol. Imaging 1 (2006) 15.
[34] Y. Kobayashi, S.C. Gu, D. Nagao, M. Konno, Curr. Nanosci. 3 (2007) 222.
[35] C. Torborg, M. Beller, Adv. Synth. Catal. 351 (2009) 3027.
[36] Y. Lu, Y. Yin, B.T. Mayers, Y. Xia, Nano Lett. 2 (2002) 183.
[37] C. Xu, K. Xu, H. Gu, R. Zheng, H. Liu, X. Zhang, Z. Guo, B. Xu, J. Am. Chem. Soc. 126 (2004) 9938.
[38] D.K. Kim, M. Mikhaylova, Y. Zhang, M. Muhammed, Chem. Mater. 15 (2003) 1617.
[39] M. Mikhaylova, D.K. Kim, N. Bobrysheva, M. Osmolowsky, V. Semenov, Thomas Tsakalakos, M. Muhammed, Langmuir 20 (2004) 2472.
[40] G. Huang, C. Zhang, S. Li, C. Khemtong, S.-G. Yang, R. Tian, J.D. Minna, K.C. Brown, J. Gao, J. Mater. Chem. 19 (2009) 6367.
[41] E.V. Shevchenko, M.I. Bodnarchuk, M.V. Kovalenko, D.V. Talapin, R.K. Smith, S. Aloni, W. Heiss, A.P. Alivisatos, Adv. Mater. 20 (2008) 4323.
[42] H. Wang, Y. Sun, Y. Yu, J. Chen, R. Li, K. Cheng, Q. Chen, Dalton Trans. 41 (2012) 346.
[43] I.P. Beletskaya, A.V. Cheprakov, Chem. Rev. 100 (2000) 3009.
[44] N. Miyaura, A. Suzuki, Chem. Rev. 95 (1995) 2457.
[45] A. Balanta, C. Godard, C. Claver, Chem. Soc. Rev. 40 (2011) 4973.
[46] L. Kong, X. Lu, X. Bian, W. Zhang, C. Wang, ACS Appl. Mater. Interfaces 3 (2011) 35.
[47] R.B. Bedford, U.G. Singh, R.I. Walton, R.T. Williams, S.A. Davis, Chem. Mater. 17 (2005) 701.
[48] A. Biffis, M. Zecca, M. Basato, Eur. J. Inorg. Chem. 2001 (2001) 1131.
[49] N. Pradhan, A. Pal, T. Pal, Langmuir 17 (2001) 1800.
[50] K. Esumi, R. Isono, T. Yoshimura, Langmuir 20 (2004) 237.
[51] P. Zhang, C. Shao, Z. Zhang, M. Zhang, J. Mu, Z. Guoab, Y. Liua, Nanoscale 3 (2011) 3357.
[52] K. Shimizua, N. Imaiidab, K. Sawabeb, A. Satsuma, Appl. Catal. A: Gen. 421–422 (2012) 114.
[53] T. Mitsudome, Y. Mikami, H. Mori, S. Arita, T. Mizugaki, K. Jitsukawa, K. Kaneda, Chem. Commun. 45 (2009) 3258.
[54] H. Woo, K.H. Park, Catal. Commun. 46 (2014) 133.
[55] Z.C. Xu, Y.L. Hou, S.H. Sun, J. Am. Chem. Soc. 129 (2007) 8698.
[56] H.R. Zhang, E.M. Meyerhoff, Anal. Chem. 78 (2006) 609.
[57] W.R. Zhao, J.L. Gu, L.X. Zhang, H.R. Chen, J.L. Shi, J. Am. Chem. Soc. 127 (2005) 8916.
[58] C.T. Chen, Y.C. Chen, Anal. Chem. 78 (2005) 5912.
[59] C.T. Chen, W.Y. Chen, P.J. Tsai, K.Y. Chien, J.S. Yu, Y.C. Chen, J. Proteome Res. 6 (2007) 316.
[60] M. Cortes, E. Gomez, J. Sadler, E. Valles, Electrochim. Acta 56 (2011) 4087.
[61] B. Liu, W. Zhang, F. Yang, H. Feng, X. Yang, J. Phys. Chem. C 115 (2011) 15875.
[62] J. Fu, M. Wang, C. Zhang, X. Wang, H. Wang, Q. Xu, J. Mater. Sci. 48 (2013) 3557.
[63] J. Zang, X. Liu, X. Guo, S. Wu, S. Wang, Chem. Eur. J. 16 (2010) 8108.
[64] F.G. de Rivera, I. Angurell, M.D. Rossell, R. Erni, J. Llorca, N.J. Divins, G. Muller, M. Seco, O. Rossell, Chem. Eur. J. 19 (2013) 11963.
[65] M.B. Gawande, P.S. Branco, R.S. Varma, Chem. Soc. Rev. 42 (2013) 3371.
[66] R. Liu, Y. Guo, G. Odusote, F. Qu, R.D. Priestley, ACS Appl. Mater. Interfaces 5 (2013) 9167.
[67] C.M. Fan, L.F. Zhang, S.S. Wang, D.H. Wang, L.Q. Lu, A.W. Xu, Nanoscale 4 (2012) 6835.
[68] Y. Choi, H.S. Bae, E. Seo, S. Jang, K.H. Park, B.-S. Kim, J. Mater. Chem. 21 (2011) 15431.
[69] H. Woo, K. Lee, K.H. Park, ChemCatChem 6 (2014) 1635.
[70] B.V. Derjaguin, L.D. Landau, Acta Physicochim. URSS 14 (1941) 733.
[71] N. Nakayama, T. Hayashi, Colloids Surf. A: Physicochem. Eng. Asp. 317 (2008) 543.
[72] Y. Wang, S. Zhang, X. Wu, Nanotechnology 15 (2004) 1162.
[73] M. Rajamathi, M. Ghoshb, R. Seshadri, Chem. Commun. 39 (2002) 1152.
[74] H. Hu, Z. Wang, L. Pan, S. Zhao, S. Zhu, J. Phys. Chem. C 114 (2010) 7738.
[75] K. Suttiponparnit, J. Jiang, M. Sahu, S. Suvachittanont, T. Charinpanitkul, P. Biswas, Nanoscale Res. Lett. 6 (2011) 27.
[76] G.A. Waychunas, C.S. Kim, J.F. Banfield, J. Nanopart. Res. 7 (2005) 409.
[77] B. Gilbert, R.K. Ono, K.A. Ching, C.S. Kim, J. Colloid Interface Sci. 339 (2009) 285.
[78] H. Zeng, A. Singh, S. Basak, K.U. Ulrich, M. Sahu, P. Biswas, J.G. Catalano, D.E. Giammar, Environ. Sci. Technol. 43 (2009) 1373.
[79] P. Bihari, M. Vippola, S. Schultes, M. Praetner, A.G. Khandoga, C.A. Reichel, C. Coester, T. Tuomi, M. Rehberg, F. Krombach, Part. Fibre Toxicol. 5 (2008) 14.
[80] Y. Jang, J. Chung, S. Kim, S.W. Jun, B.H. Kim, D.W. Lee, B.M. Kim, T. Hyeon, Phys. Chem. Chem. Phys. 13 (2011) 2512.
[81] M. Zhu, G. Diao, J. Phys. Chem. C 115 (2011) 24743.
[82] R. Li, P. Zhang, Y. Huang, P. Zhang, H. Zhong, Q. Chen, J. Mater. Chem. 22 (2012) 22750.
[83] H. Woo, J.W. Kim, M. Kim, S. Park, K.H. Park, RSC Adv. 5 (2015) 7554.
[84] A.M. Karim, V. Prasad, G. Mpourmpakis, W.W. Lonergan, A.I. Frenkel, J.G. Chen, D.G. Vlachos, J. Am. Chem. Soc. 131 (2009) 12230.

Please cite this article in press as: H. Woo, K.H. Park, Recent developments in hybrid iron oxide–noble metal nanocatalysts for organic reactions, Catal. Today (2016), http://dx.doi.org/10.1016/j.cattod.2016.01.030

[85] Y. Deng, Y. Cai, Z. Sun, J. Liu, C. Liu, J. Wei, W. Li, C. Liu, Y. Wang, D. Zhao, J. Am. Chem. Soc. 132 (2010) 8466.
[86] G.M. Scheuermann, L. Rumi, P. Steurer, W. Bannwarth, R. Mülhaupt, J. Am. Chem. Soc. 131 (2009) 8262.
[87] S.Y. Gan, M. Chow, J. Mater. Chem. 14 (2004) 2781.
[88] P.V. Kamat, J. Phys. Chem. Lett. 2 (2011) 242.
[89] D. Su, H.-J. Ahn, G. Wang, Chem. Commun. 49 (2013) 3131.
[90] H. Xu, Q. Yang, F. Li, L. Tang, S. Gao, B. Jiang, X. Zhao, L. Wang, C. Fan, Analyst 138 (2013) 2678.
[91] A.P. Grosvenor, B.A. Kobe, M.C. Biesinger, N.S. McIntyre, Surf. Interface Anal. 36 (2004) 1564.
[92] D. Yang, A. Velamakanni, G. Bozoklu, S. Park, M. Stoller, R.D. Piner, S. Stankovich, I. Jung, D.A. Field, C.A. Ventrice Jr., R.S. Ruoff, Carbon 47 (2009) 145.
[93] R. Massart, IEEE Trans. Magn. 17 (1981) 1247.
[94] J.-B. Moussy, J. Phys. D: Appl. Phys. 46 (2013) 143001.
[95] M. Turner, V.B. Golovko, O.P.H. Vaughan, P. Abdulkin, A. Berenguer-Murcia, M.S. Tikhov, B.F.G. Johnson, R.M. Lambert, Nature 454 (2008) 981.
[96] X. Meng, B. Li, X. Ren, L. Tan, Z. Huang, F. Tang, J. Mater. Chem. A 1 (2013) 10513.
[97] X. Chen, Z. Cai, X. Chen, M. Oyama, J. Mater. Chem. A 2 (2014) 5668.
[98] C. Wang, H. Daimon, S. Sun, Nano Lett. 9 (2009) 1493.
[99] Z. Liu, X. Gong, J. Kohanoff, C. Sanchez, P. Hu, Phys. Rev. Lett. 91 (2003) 266102.
[100] H. Woo, J.C. Park, S. Park, K.H. Park, Nanoscale 7 (2015) 8356.
[101] X. Zhang, C. Niu, Y. Wang, S. Zhou, J. Liu, Nanoscale 6 (2014) 12618.
[102] W.-P. Li, P.-Y. Liao, C.-H. Su, C.-S. Yeh, J. Am. Chem. Soc. 136 (2014) 10062.
[103] A. Kirkeminde, S. Ren, Nano Lett. 14 (2014) 4493.
[104] J. Mao, X. Cao, J. Zhen, H. Shao, H. Gu, J. Lu, J.Y. Ying, J. Mater. Chem. 21 (2011) 11478.
[105] V. Mazumder, M. Chi, K.L. More, S. Sun, J. Am. Chem. Soc. 132 (2010) 7848.
[106] Y. Yu, K. Sun, Y. Tian, X.-Z. Li, M.J. Kramer, D.J. Sellmyer, J.E. Shield, S. Sun, Nano Lett. 13 (2013) 4975.
[107] X. Liu, J. Zhang, L. Wang, T. Yang, X. Guo, S. Wu, S. Wang, J. Mater. Chem. 21 (2011) 349.
[108] Q.Q. Xiong, J.P. Tu, Y. Lu, J. Chen, Y.X. Yu, Y.Q. Qiao, X.L. Wang, C.D. Gu, J. Phys. Chem. C 116 (2012) 6495.
[109] S. Guo, S. Zhang, X. Sun, S. Sun, J. Am. Chem. Soc. 133 (2011) 15354.
[110] L. Wang, W. Yi, C. Cai, Chem. Commun. 47 (2011) 806.
[111] C. Rossy, J. Majimel, E. Fouquet, C. Delacôte, M. Boujtita, C. Labrugère, M. Tréguer-Delapierre, F.-X. Felpin, Chem. Eur. J. 19 (2013) 14024.
[112] B. Panda, T.K. Sarkar, Chem. Commun. 46 (2010) 3131.
[113] L.A. Jones, S. Sanz, M. Laguna, Catal. Today 122 (2007) 403.
[114] L. Yu, X. Jiang, L. Wang, Z. Li, D. Wu, X. Zhou, Eur. J. Org. Chem. 2010 (2010) 5560.
[115] P. Li, L. Wang, M. Wang, F. You, Eur. J. Org. Chem. 2008 (2008) 5946.
[116] J.E. Perea-Buceta, T. Wirtanen, O.-V. Laukkanen, M.K. Mäkelä, M. Nieger, M. Melchionna, N. Huittinen, J.A. Lopez-Sanchez, J. Helaja, Angew. Chem. Int. Ed. 52 (2013) 11835.
[117] H.R. Choi, H. Woo, S. Jang, J.Y. Cheon, C. Kim, J. Park, K.H. Park, S.H. Joo, ChemCatChem 4 (2012) 1587.
[118] J.C. Park, E. Heo, A. Kim, M. Kim, K.H. Park, H.J. Song, J. Phys. Chem. C 115 (2011) 15772.
[119] H. Woo, K. Lee, J.C. Park, K.H. Park, New J. Chem. 38 (2014) 5626.
[120] M.B. Gawande, P.S. Brancoa, R.S. Varma, Chem. Soc. Rev. 42 (2013) 3371.

Please cite this article in press as: H. Woo, K.H. Park, Recent developments in hybrid iron oxide–noble metal nanocatalysts for organic reactions, Catal. Today (2016), http://dx.doi.org/10.1016/j.cattod.2016.01.030